Fall 2014

Performance evaluation of coaxial horizontal axis hydrokinetic turbines system

Abdulaziz M. Abutunis

Department:

PERFORMANCE EVALUATION OF COAXIAL HORIZONTAL AXIS HYDROKINETIC TURBINES SYSTEM

by

ABDULAZIZ ABUTUNIS

A THESIS

Presented to the Faculty of the Graduate School of the

MISSOURI UNIVERSITY OF SCIENCE AND TECHNOLOGY

in partial Fulfillment of the Requirements for the Degree

MASTER OF SCIENCE IN MECHANICAL ENGINEERING

2014

Approved by

K. Chandrashekhara, Advisor
Xiaoping Du
Jonathan Kimball

ABSTRACT

Hydrokinetic energy technologies are emerging as a viable solution for renewable power generation. Unlike conventional hydropower turbines, hydrokinetic turbines are environmentally friendly; they operate at zero-head, and do not need dams to preserve the water. Unfortunately, they have a low efficiency which makes their design a challenging task. This work was focused on the hydrodynamic performance of horizontal axis hydrokinetic turbines (HAHkTs) under different turbine arrangements and flow conditions.

It was undertaken in an effort to improve the efficiency of small HAHkTs that harness a river's kinetic energy. Four sets of experiments were performed in a water tunnel to investigate small-scale constant cross-section HAHkT models with various configurations. The first set of experiments provided insight into the operating characteristics of a 3-blade single turbine by varying its pitch angle (θ) , tip speed ratio (TSR), flow speed (U_∞), and applied load. A multi-turbine system of both two and three 3- blade rotors (mounted coaxially to the same shaft) was tested in the second set of experiments. The purpose was to decrease the turbine system solidity while increasing the blade number. Here, the number of and the distance between rotors as well as the rotors relative installation angle were investigated. A long duct reducer was used to shroud single turbine and multi- turbine system in the third set of experiments. The particle image velocimetry (PIV) technique was used in the final set of experiments to examine the flow patterns at different axial locations downstream from two different turbine configurations. The effect of the flow speed on the wake characteristics was also examined in this experiment.

ACKNOWLEDGMENTS

I would like to express my profound sense of gratitude and sincere appreciation to my advisor Dr. K. Chandrashekhara, for his encouragement, guidance, and support throughout my study and research. He has always been a great source of wisdom and confidence and without him this thesis would not have been completed.

I would also like to express my sincere gratitude to the members of advisory committee, Dr. Xiaoping Du and Dr. Jonathan Kimball for their support, cooperation and their valuable time.

The author would like to acknowledge the financial support received from the Department of Mechanical and Aerospace Engineering at Missouri University of Science and Technology and the support of the Office of Naval Research (Grant # N000141010923). Also, the support from the Libyan Ministry of Higher Education for their sponsorship provided during my Master study is gratefully acknowledged.

I would also like to extend my acknowledgement to my fellow members: Haifeng Li, Gregory Taylor, and James Nicholas for sharing useful thoughts and engaging in fruitful discussions over the duration of this work. I also would like to acknowledge my colleague Mohaned Mohamed for all the work we have done in the composite housing area research. My thanks are extended to my other follow members for their help and advice. I would also like to acknowledge Abdulhakim Jabbr, my best friend, for his continuous help and for making my life in Rolla memorable. I sincerely thank the machine shop staff for all the help in building the experimental set-up.

Last, but certainly not least, I would like to thank my wife, my parents, my elder brother, and all my family members for their constant support, cooperation and love.

TABLE OF CONTENTS

Page

LIST OF ILLUSTRATIONS

Page

LIST OF TABLES

Page

1. INTRODUCTION

1.1. IMPORTANCE OF RENEWABLE ENERGY

Energy is an essential element to both economic and social development. It plays a pivotal role in improving a society's standard of living. The need for energy has grown rapidly as an increasing world population pushes industrial expansion and energy demand [1]. The greatest demand is focused on electricity. A large percentage of the world's electricity and other energy generation is based on conventional fuel [2]. The current trend of consuming conventional energy has generated a great deal of concern regarding energy sustainability.

Renewable energy has become well-known as an alternative solution for conventional energy concerns. Hydropower, wind, solar radiation, geothermal, photosynthesis, and biomass are each considered primary renewable energy resources with auspicious power generation capability. Due to the diversity in the renewable energy resources, there is abundance in their technology options and applications, as well as their availability all over the word [3]. Therefore, this makes them an important component of energy supply that will pushes the world to more secure and sustainable energy path [4].

1.1.1. Energy Scenario. A major portion of the world's energy demand is currently being met by fossil fuels (e.g., coal, petroleum, and natural gas).Unfortunately, these fuels decrease gradually with each passing day. The combustion of fossil fuels for energy generation is the primary source of carbon dioxide emissions. The global consumption of energy in 2005 was 411EJ (approximately 389.553 quadrillion Btu per year), 94% of which was met by fossil fuels. The remaining 6% was met by nuclear and renewable energies [5]. North America was responsible for 27% of the overall energy consumed [5]. Figure 1.1 illustrates the growth history of the primary energy consumed of various fuel categories between 1965 and 2005.

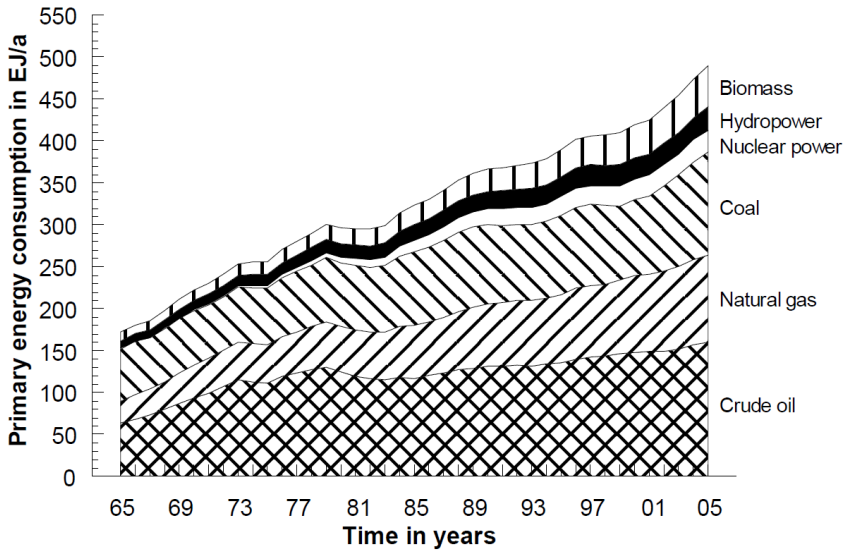

Figure 1.1. Worldwide primary energy consumption [5]

According to World Energy Outlook 2010 [4], between 2008 and 2035, the world's primary energy demand increased by 36% (a yearly average of 1.2%). During this same period, the emissions produced by consuming (burning) this amount of energy jumped from 29 Gt (Gugatonne) to 35 Gt. Despite the technology advances to increase the efficiency and reduce the energy consumption and related emission, the trends of the energy-related CO2 usage indicate increment of the earth temperature in the future by 6o. This increase in the global temperature will affect the economy and environment tremendously [3].

Approximately 4.7% of the world's total population lives in the United States. This population consumes nearly 22.5% of the world's energy each year. Recent studies have shown that, of the U.S. total energy consumed in 2012 (95.02 Quads or quadrillion Btu), only 7.5% was met by renewable energy resources. The annual rate of growth of primary renewable energy is predicted to be about 1.6 % throughout the next 28 years. Thus, by 2040, the primary renewable energy will be responsible for 10% (11.05 Quads) of the total energy consumed in the U.S. (see Figure 1.2). This rate of growth of the renewable energy technology seems promising. Nevertheless, by 2040, the dependency on fossil fuels for energy generation (in the U.S.) will still dominate at approximately 80% (a total consumption of 86.46 Quads). During this same period, energy prices,

driven by different factors, are expected to fluctuate. Overall, they expected to grow through 2040 [6].

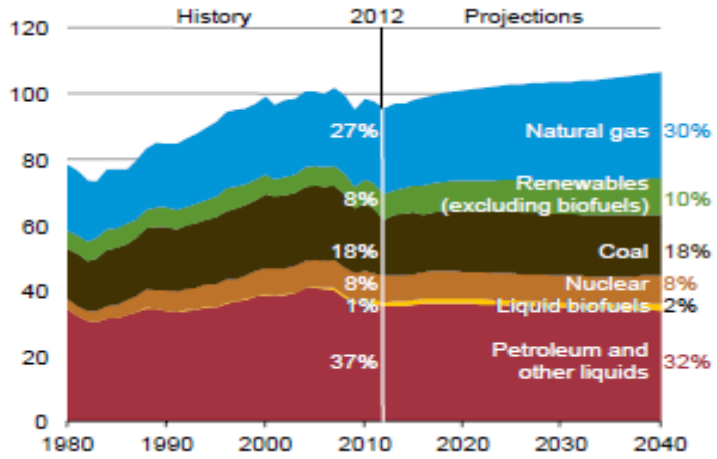

Figure 1.2. Primary energy consumption in the United States (in Quads) [6].

The excessive production of energy resources cannot be sustainable [1]. A number of researchers have offered a timeframe in which they predicted these fuels will become depleted. Lior [7] estimated that, if the current production of fossil fuels continues at the same level, oil will become depleted in 40 years, natural gas will become depleted in 60 years, and coal will become depleted in 150 years. Consider of all these above-mentioned facts, energy sustainability, price increment, and climate effects are obvious challenging issues that emphasize the essential role of renewable energy. Consequently, this necessitates urgent effort by the world's governments to extenuate the current usage rate of fossil fuels and spend more of their budget to subsidize the renewable energy technology.

1.1.2. Renewable Electricity in the United States. There is consensus that the use of renewable energy to compensate the energy deficit is inevitable. Electricity generation using renewable resources is considered the most valuable technology for investigation[8]. Under the New Policies Scenario [9], the world's renewable energy usage, in general, grows by a factor of 3 between 2008 and 2035, and its participation in

electricity generation increases from approximately 19% to 33%. This increase in the renewable electricity is dominated by the hydropower followed by the wind energy [9]. Electric Power Research Institute (EPRI) [10] noted that the economic growth and electricity demand in the U.S. are coupled. According to the AEO2014 Reference case [6], the electric power sector in the U.S. is responsible for 40% of the country's total primary energy consumption. This electrical energy consumption grows by an annual rate of 0.9% between 2012 and 2040. This growth indicates that, the electricity consumed jumps from 3,826 billion kWh in 2012 to 4,954 billion kWh in 2040. Renewable energy (including the conventional hydropower) was responsible for 12% of the total annual electricity generated in 2012 in the U.S. This share is expected to increase to 16% by the end of the projection period (2040) [6]. Based on EPRI [10], in 2011, 63% of the renewable electricity energy used was produced by hydropower.

Figure 1.3 illustrates the electricity produced by energy source in the U.S. in 2011. Hydropower comprised 7.9% of this electrical energy generation. This ratio accounts for 63% of the renewable electricity generation. Wind and solar energy sectors showed faster growth during the last few years. [11]. Figure 1.3 also indicates that, in general, the renewable energy comprised a relatively small portion of the electricity generation sector. The reason is attributed to that, even though renewable resources are good candidate for addressing the environmental and energy security concerns, their prices, in term of kWh cost, is relatively high compared with conventional energy resources like fossil fuel.

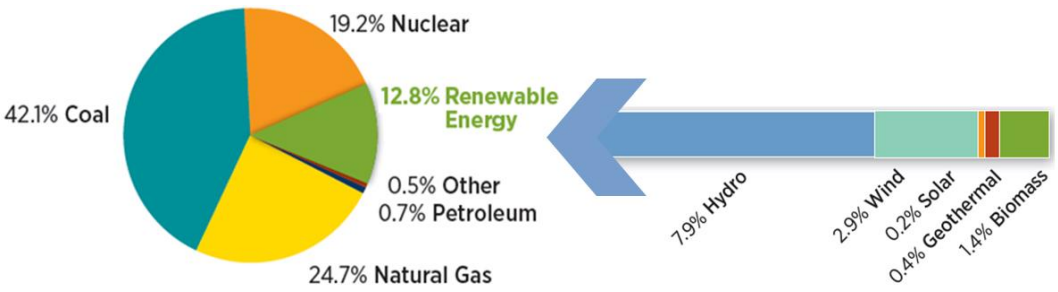

Figure 1.3. Electricity generation by energy source in the U.S. during 2011 [11]

From the economic aspect, initial costs of energy (COE) that have been calculated for hydrokinetic turbines are quite promising. Unlike the wind turbine systems that require an expensive yawing mechanism controller due to the wind changeable directions, hydrokinetic turbines are mounted firmly, facing the unidirectional flow stream. Moreover, performance enhancement of wind turbine using duct has considerable disadvantage due to additional weight and drag that carried by the turbine tower. These undesired extra loads require proper design and stronger materials and thus more costs. In contrary, these issues are of less concern in hydrokinetic turbines. Hydrokinetic systems also offer higher energy generation per unit square of rotor swept area. In some instances, the power generated may reach four times that of the similarly rated power wind turbines. Finally, hydrokinetic systems do not require dams or powerhouse, easing and accelerating the system's deployment while reducing final costs [12-15].

In long-term operation, the overall cost of energy generated by hydrokinetic system is relatively low. For example, 10 kW hydrokinetic turbine unit operates for 15 years, with assumption of yearly maintenance cost to be $1000, would results in 4 years to cover its investment cost [16].

1.1.3. The Hydrokinetic Energy Potential in U.S. Rivers. The kinetic energy present in flowing water is considered a rich source of hydro-renewable energy [17].The United States is abundant with rivers. Over 250,000 rivers comprise 3.5 million miles of waterways across the nation. Stated by [18, 19], the yearly theoretical and technically coverable hydrokinetic energy of the rivers in United States is 1381TWh and 119.9TWh, respectively. The Midwest, in particular, is overlaid with a number of these rivers and waterways. The Missouri River, a branch of the Mississippi River, is the longest of these waterways with a length of 2,540 miles. The Mississippi River, which crosses the northern portion of Missouri (by approximately 400 miles) has the highest flow volume [18, 19]. The kinetic energy existed in flowing rivers is dependent on flowing medium density, flow velocity, and cross-sectional area of the river. The theoretical kinetic energy can be calculated as

$$P = \frac{1}{2}(\rho AV)V^2 = \frac{1}{2}\rho AV^3 \quad (1)$$

where the water density (ρ) is equal to $997.048\ \mathrm{kg/m^3}$, the area through which the flow passes is (A), and the water flow velocity is V. For hydrokinetic turbines, A represents the rotor swept area. Hydrokinetic turbines operated in rivers need a minimum current speed of 1-2m/s. A number of technological approaches can lower this speed to 0.5m/s. Optimum operational flow speeds are between 1.5 and 3.5 m/s. These turbines also require specific water depth for optimizing its operation [20].

A Large portion of streams flow down low depth rivers, and the kinetic energy dissipates [21]. The deployment of hydrokinetic turbines in the neighboring river basins will offer significant economic advantages to the local communities. However, several technical, economical, and environmental issues must be overcome before these systems can be used on a commercial scale [20].

1.2. HYDROPOWER TURBINES

1.2.1. Historical Review of Hydropower Turbines. A concise historical overview of the hydropower usage would facilitate chronology of advent and evolution of these convertor systems[22]. Some of the earliest machines humans have utilized were operated by the energy contained in mobile water. These machines evolved over centuries; humans have been studying and developing them for decades. The water-mill is a structure that uses a water-wheel and is believed to have been invented in either the fourth or third century B.C. The water-mill is considered as one of the most ancient of these convertor machines. The earliest existing water-mill, found in Venafro in southern of Italy, has been back dated to the Roman Empire [23]. Using a wheel as a rotor of water-mill, the ancestors of this water-wheel were developed to grind grains and lift water to canals for both human consumption and irrigation. Figure 1.4 is a photograph of well-preserved ancient water-wheel (called Noria). It was invented by the Romans and was used to lift the water into small aqueducts to irrigate the fields around the city of Hama in Syria [24].

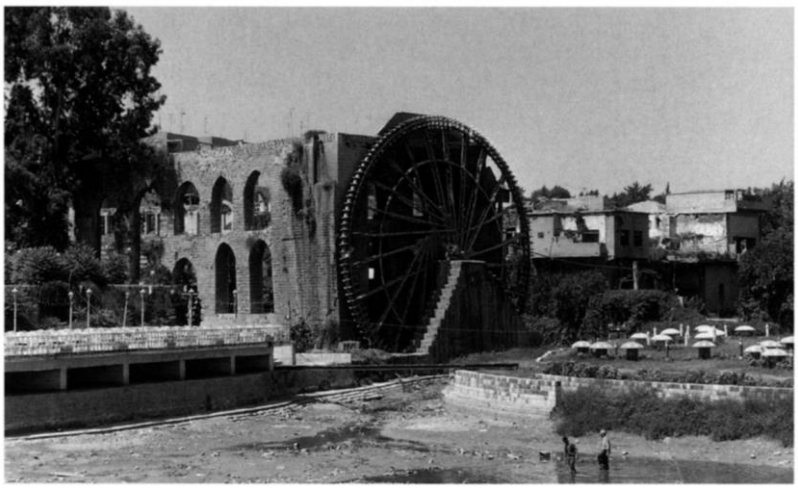

Figure 1.4. Noria water-wheel in Hama, Syria [24]

The conversion from the water-mill to the contemporary hydropower turbine (or water turbine) occurred during the industrial revolution when specific philosophies and methods were applied. In the 19th century, before the emergence of electrical grids, the developed water-wheel technology was used to power factories that produced textiles and wood products. More recently, as the contemporary civilization realized the essential role of the electrical power, the hydropower converters emerged as a key option for power generation during the middle of 19th century. Recently, different hydropower turbines with various sizes and types are developed and started to appear all over the world. This machine is a clear example of humans utilizing nature to operate a machine [24, 25].

1.2.2. Classification of Hydropower Turbines. Hydropower turbines are converter devices that rotate by harvesting energy from flowing water to produce a mechanical power in form of torque and rotational speed. Hydropower turbines can be designed to work in different water environments. Two important parameters must be considered when choosing the turbine to be used: the water head and the flowing volume. Turbines that need a large hydraulic head and a small water flow volume are known as classical (conventional) turbines. For these turbines to operate, the potential energy of water with high head needs to be converted to kinetic energy. This kinetic energy, then, used to rotate their rotors. Turbines that depend on the water flow volume to operate are known

as hydrokinetic turbines. These turbines harvest the kinetic energy directly from the flowing water and then convert that energy to rotational mechanical energy.

Classical turbines have served as a consistent energy resource for a long time. Currently, this resource comprises approximately 10% of the total energy consumed in the U.S. [21]. Moreover, classical turbines are considered to be more efficient than hydrokinetic turbines. Nevertheless, classical turbines require construction of dams. These dams are confined to the bonds of high cost, sit availability, and environmental impact that dams may cause to the water inhabitants [26]. Consequently, classical turbines are not adequate to meet the increasing demand for energy. Therefore, interest in hydrokinetic turbines has grown gradually in the last decade. This interest in hydrokinetic turbines was owing to two reasons: these systems offer the ability of extracting energy from rivers under zero-head, and they are easy to be deployed at various rivers sits [22, 27].

1.3. HYDROKINETIC TURBINES

1.3.1. Hydrokinetic Turbines: A General View. Hydrokinetic turbines are designed to be deployed in rivers, converting the passing stream's kinetic energy into mechanical energy. It then uses a generator to convert the mechanical energy into electrical energy. The operational principle of the hydrokinetic turbine (see Figure 1.5) is similar to the wind turbine. The range of a river's current speed is 1-3 m/s which is lower than that of the wind (11-13 m/s). However, the water is 850 times denser than air. Therefore, hydrokinetic turbines are exposed to higher kinetic energy than wind turbines are exposed to under the same rotor swept area [8, 28]. Horizontal axis hydrokinetic turbines (HAHkTs) and vertical axis hydrokinetic turbines (VAHkTs) (also known as cross flow turbines) are the hydrokinetic turbines most often used. These turbines are categorized according to their rotational axes with respect to the water current's direction [29]. Horizontal axes hydrokinetic turbines have rotational axes that are parallel to the flow direction. In contrast, vertical axis hydrokinetic turbines rotate normal to the flow [30, 31]. According to Khan et al. [32], these hydrokinetic turbines can also be classified based on their lift and drag characteristics

The literature on hydrokinetic energy conversion systems is quite extensive. For example, Güney and Kaygusuz [8], Kahn et al. [22, 27, 32], and Lago, Ponta, and Chen [33] each offered detailed insight into the various types of hydrokinetic turbines that are available, the environment in which they operate, instillation preferences, and their sizes and capacities. They also discussed both the advantages and disadvantages of these systems. Kahn et al. [22, 27] introduced specific information on various river and tidal current conversion systems. Furthermore, the use of duct also has been investigated by the researchers. Higher improvement has been shown when the duct was used with VAHkTs rather than the HAHkTs. Lago et al. [33] investigated the most recent hydrokinetic system development. They confirmed that, the future challenge of conversion system design exceeds the classical consideration of the mere enhancement of the system's performance. It is to achieve that optimized performance with additional attention toward the economy and environment. Güney and Kaygusuz [8] listed various axial and vertical hydrokinetic turbines with detailed information on their geometry, power output, operational environment, and manufacturers. Several types of different hydrokinetic conversion systems (HAHkTs and VAHkTs) are illustrated in figure 1.6.

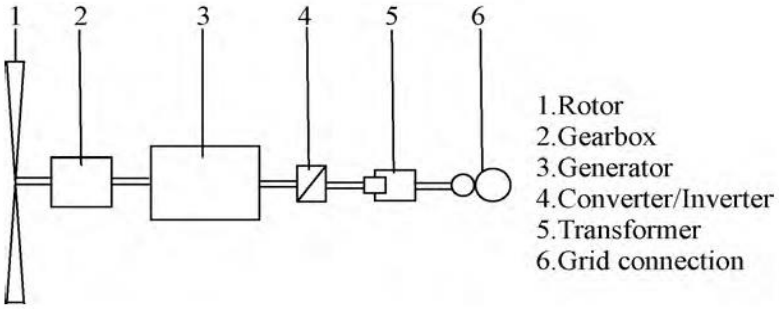

Figure 1.5. Principle scheme of a hydrokinetic turbine system [8]

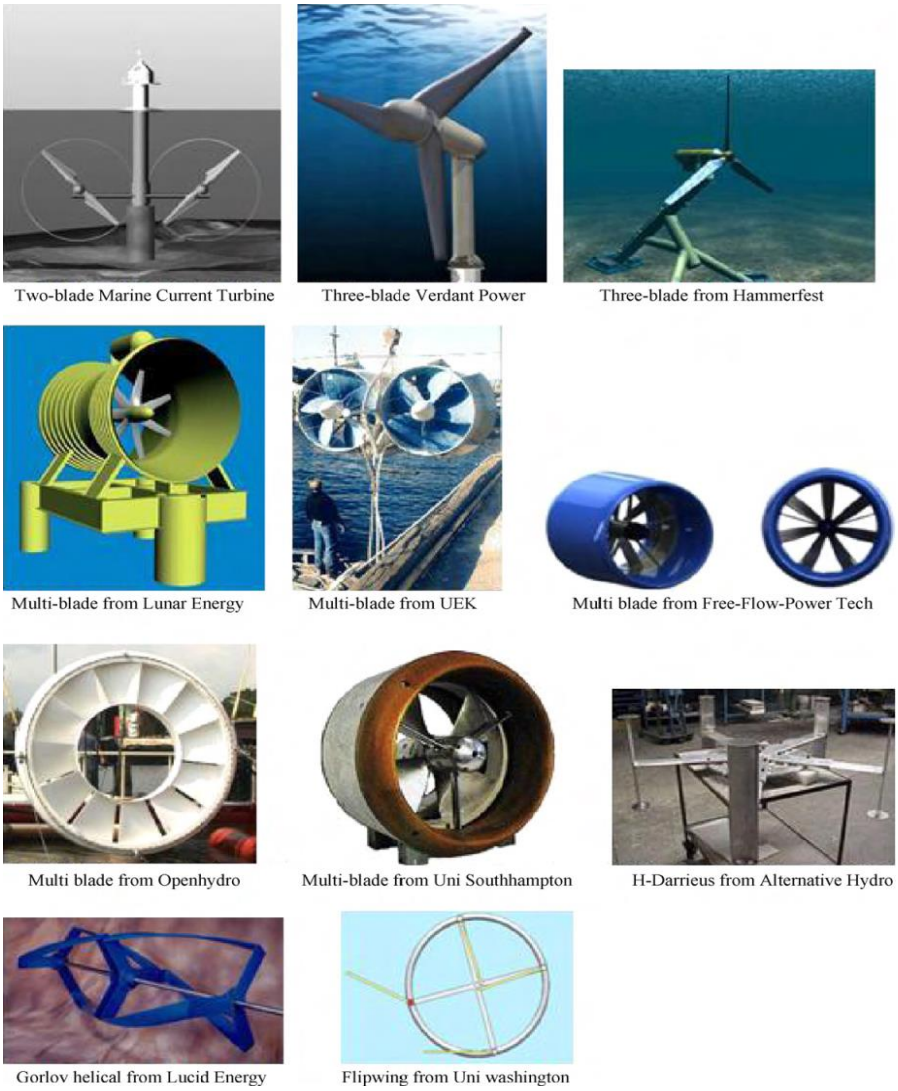

Figure 1.6. Various hydrokinetic turbines [8]

Preferably, hydrokinetic turbines sit close to the water's surface where the energy flux is higher and more kinetic energy can be captured. Unfortunately, this positioning may not be possible due to various marine activities, including marine transportation and fishing. Bridge and culvert structures may also prevent this placement. [27]. The general classification of several common hydrokinetic turbines is given in Figure 1.7. This classification is based on the turbine's physical configuration.

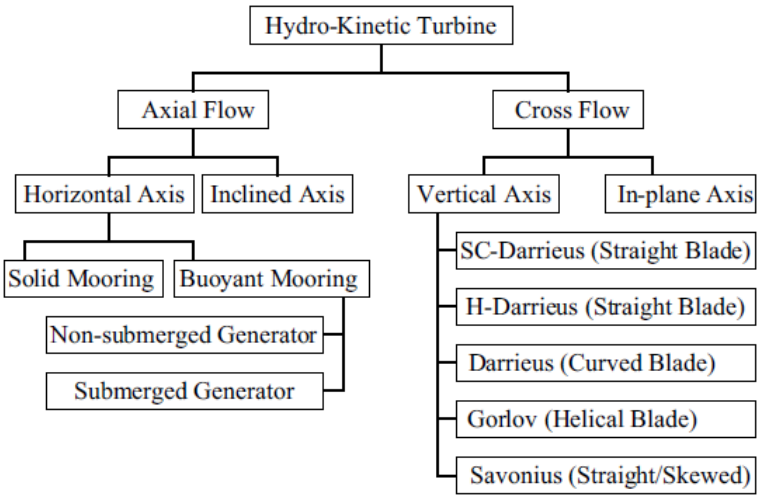

Figure 1.7. General classification of hydokinetic turbines [32]

1.3.2. A Comparison Between HAHkTs and VAHkTs. Even though hydrokinetic turbines, generally, operated on the same conversion principles, a number of differences may appear in forms of design and operational features. The VAHkTs are characterized by the ease of design and generator coupling. They also emit less noise into the ambient environment [27]. In contrast, HAHkTs are superior in terms of performance and control [34]. Knowledgebase comes from the fact that HAHkTs share similar principle characteristic with wind turbines is another advantage. This similarity allows for technology transfer to the HAHkTs with taking into account the free surface effects and the cavitation phenomenon [35].

Unlike HAHkTs (which are inherently self-starting), VAHkTs typically need a mechanism that initiates the turbine's rotation [8]. Moreover, due to the orthogonality of the VAHkT rotor and flow stream, a VAHkT's blades will face the flow stream periodically, producing a ruffle in the output torque [32].

Both design characteristics and initial costs play a key role in the success of the new hydrokinetic turbine technologies which the HAHkTs lack. Typically, a HAHkT's blades are designed to have twist and taper (profile and distal), which require careful machining and manufacturing. From a performance standpoint, these blades allow for uniform lift force distribution, producing higher efficiency, lower fatigue loading, and

lower cavitation than their counterparts [17]. Therefore, these features HAHkTs have may decrease the overall long-term costs. Based on the aforementioned facts, the HAHkTs might be considered as viable option for the hydrokinetic power generation with the consideration of the long-term cost per kilowatt-hour. Table 1.1 summarizes several of the differences between HAHkTs and VAHkTs.

Table 1.1. A comparison between HAHkTs and VAHkTs

Features	HAHkTs	VAHkTs
Instillation	Flexible system mounting. This systems can be mounted at different altitudes: -Bottom structure mounting (BSM) -Floating structure mounting (FSM) -Near surface arrangements (NSM).	Primarily instilled with a near surface arrangement (NSM), allowing the generator to be placed above the water level.
Self-starting	Blades are designed to have taper and twist. This design allows for uniform lift force distribution and thus less fatigue loading and cavitation. Turbines are also self-starting with using this design.	Blades are typically designed to have a constant cross-section. These turbines face the flow periodically and thus suffer from either low or negative torque. This low torque prevents the turbine from accelerating up to operating speeds. Moreover. These turbines always need a starter.

Table 1.1. A comparison between HAHkTs and VAHkTs (cont.)

Features	HAHkTs	VAHkTs
Vibration	This system is not subjected to any vibrations produced by continuously changing angles of attack.	These turbines' blades are subjected to cyclic tangential pulls and generate significant torque ripples at the output. Serious problems can occur if frequency of vibration coincides with the resonant frequency of the support structure.
Efficiency	This system retains a higher efficiency due to lower incidence losses[1].	The flow enters over one-half of the periphery radially inward and emerges over its other half flowing radially outward. The velocity near the center of the vortex is higher than the velocity further away from the center, resulting in a lower efficiency

[1] Loss refers to any work done in turning the working fluid from its direction of approach to the rotor to the direction required by the blade's passage.

1.4. SCOPE OF THESIS

Optimizing an HAHkT system's efficiency is a significant challenge. Factors considered to optimize the hydrokinetic turbine's performance include the following:

- Rotor configuration
- Number of blades
- Number of rotors in the turbine system (this is specific for this study)
- Material chosen for the turbine system components
- Proper gearing and bearing mechanism

This study was conducted in an attempt to enhance HAHkT's efficiency and thus increase the power generated from the river's current.

This thesis is organized into five main sections. Section 1 is a discussion on the importance of renewable energy. It includes an energy scenario that confirms that most of energy comes from conventional fuels. The section also includes a discussion on the renewable electricity in the United States. The turbines used in this research were specified for generating electricity from the rivers. Thus, more consideration is given to the hydropower (specifically hydrokinetic) renewable energy than the other forms of renewable energies. Section 1 also includes general review about the hydropower turbines and their types. The hydrokinetic turbine is discussed in more details in terms of installation and types. Finally, some advantages and disadvantages of different hydrokinetic kinds are examined.

An HAHkT's hydrodynamics are discussed in section 2. This discussion includes principle definitions on number of hydrodynamic governing parameters and design factors used throughout this thesis. Two important phenomena are also investigated and explained: the wake in the downstream regions and the stall around the rotating blades. These two phenomena contribute to the turbine system's efficiency. The section ends with not only a review of previously conducted studies but also the objectives of the work.

Section 3 details both the used experimental apparatus and hydrokinetic energy conversion system's design. It also addresses the methods used to acquire the experimental data to determine the power output (e.g., RPM sensor and the torque

sensor). The flow visualization process and the utilized tools (PIV system setup) used in water tunnel calibration and wake investigation are also discussed in detail. A portion of this section includes the conducted primary calibrations for both water tunnel and sensors. This section also contains a description of the experimental setup and hydrokinetic conversion systems' configurations (e.g., single and multi-turbine systems, pitch angle, rotors arrangements for multi-turbine system, ducted turbine systems, and unducted turbine systems).

Section 4 presents the results of the investigation. The power and power coefficient curves generated by different turbine configurations and setups were presented and analyzed (e.g., three- and six-blade single turbines, three -blade single and multi- ducted and unducted turbine systems). The flow visualization results are also discussed within this section.

Section 5 includes a summary of the research conducted and the results gathered. Recommendations for future work are also made in this section.

2. HAHkTs HYDRODYNAMICS

2.1. HYDRODYNAMIC DESIGN PARAMETERS OF HAHkTs

A hydrokinetic turbine's performance can be characterized by both its power and its power coefficient. Hydrokinetic turbines inherently exhibit a low efficiency, a primary obstacle to commercializing this technology [36]. Enhancing an HAHkT's performance is a challenging task requires an advance understanding of various interrelated design parameters (e.g., solidity, number of blades, tip speed ratio, rotational speed of the rotor, pitch angle, and angle of attack). Moreover, an HAHkT's performance is affected by the flow characteristics, such as incident flow stream (free-stream velocity average) and free-stream turbulence.

2.1.1. Principle Definitions. Important hydrodynamic parameters are presented and discussed in this section.

Pitch angle (θ) and angle of attack (AoA or α): Pitch angle is the angle between the blade chord and the turbine plane of rotation. It is used to adjust both the rotational speed and generated power. The local angle of attack (AoA) is defined as the angle between the local relative flow (U_r) and the blade chord. A turbine's optimum AoA is more complicated than a plane wing. The optimum design of AoA for a wing occurs when the lift to drag ratio is at a maximum. This optimized design of AoA is more sophisticated in turbines because the AoA changes along the blade span. This change occurs because AoA is a function of the angular velocity and the radial distance from the rotor's center. The radius effect results in stall at the blade sections close to the hub [37]. Figure 2.1 illustrates the pitch angle and AoA (AoA is referred to as α in the figures and equations) without considering the induction factors. Local AoA (α_r) can be calculated from the pitch angle, the incoming axial velocity, the radial distance from the rotor's center, and the rotor's rotational velocity. Equations 2 and 3 help highlight the relationship between these variables.

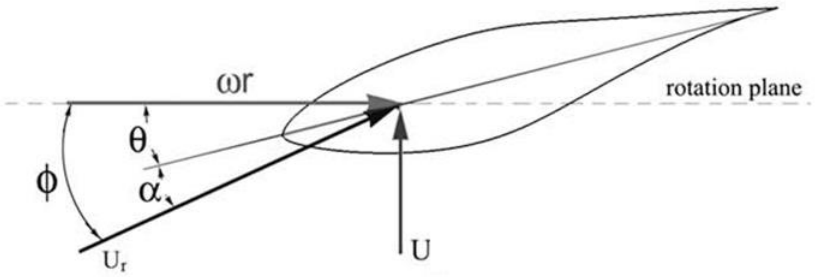

Figure 2.1. Pitch angle and angle of attack [37]

The local AoA at a section located at radial distance r form the rotor's center is:

$$\alpha_r = arctan(\phi_r) - \theta \tag{2}$$

where, ϕ_r is the angle between the local relative flow that seen by the hydrofoil and the rotor plane of rotation. This angle is defined as

$$\phi_r = \frac{U}{\omega . r} \tag{3}$$

where U is the axial free stream velocity, ω is the angular velocity of the rotor, and r is the radial distance from the rotor's center (a radial distance at which the relative velocity U_r and the AoA are considered).

Viscous effects and axial and tangential induction factors (a, and a'): can be used to calculate a 2-D equivalent angle of attack [38]:

$$\phi_r = \frac{(1-a)U}{(1+a')\omega . r} \tag{4}$$

Axial and tangential induction factors (a, and a′): An axial induction factor can be obtained from the actuator disk theory to define an equivalent reduced flow velocity (created by flow that escapes to the ambient) at the rotor's plane. The axial induction factor is defined as the ratio of reduction of the flow velocity that occurs when flow passes through the rotor to the undisturbed flow velocity:

$$a = \frac{U - U_x}{U} \tag{5}$$

Here U_x is the decreased axial velocity in the downstream, behind the rotor. The tangential induction factor (a') is a fractional increase in the angular velocity. This attributed to the increased angular velocity at the blades from the conservation of momentum. The a' can be given as a function of a:

$$a' = \frac{1 - 3a}{4a - 1} \tag{6}$$

Tip speed ratio (TSR): The tip speed ratio is an important parameter to consider when designing hydrokinetic turbines because the power coefficient is affected by this ratio. It is also adequate when comparing similar turbines with different sizes [39]. The tip speed ratio is defined as the ratio of the blade tip tangential speed to the incoming flow velocity:

$$TSR = \frac{\omega R}{U} \tag{7}$$

where ω is the angular velocity of the rotor, R is the radius of the rotor, and U is the free stream velocity.

Number of blades (N) and solidity (σ): Turbine solidity is proportional to the number of blades and the blade chord length. It is defined as the ratio of the total chord length of all of the blades to the circumference of the turbine:

$$\sigma = \frac{Nc}{2\pi R} \tag{8}$$

where N is the number of blades, c is the blade chord length, and R is the turbine's radius.

Lift (L) and drag (D) forces: The hydrodynamic forces exerted by the incoming flow on the turbine blades are produced by the pressure difference between blade's upper and lower surfaces as well as the viscous stresses. Pressure force acts normal to the blade's surface while the viscous stresses act both normal and tangent to the blade's surface. The

viscous force's contribution to the normal force is minor when compared to the pressure forces. Thus it can be neglected. The net force component, parallel to the relative velocity direction (U_r), is the drag force (D). The force component, normal to the relative flow direction, is the lift force (L). The viscous forces contribute, primarily, to the drag. The pressure forces, however, have a lift and a drag component. The drag that is produced by pressure becomes extremely large when the hydrofoil stalls [38, 40]. (For a more in-depth discussion on the stall phenomenon, see Section 2.2).

Lift coefficient C_L and drag coefficient C_D are non-dimensional parameters that associate, respectively, the lift force and drag force to the flow density, velocity around the blade, and associated reference area. In hydrokinetic turbines, these coefficients are affected by the angle of attack. They are expressed as

$$C_L = \frac{L}{\frac{1}{2}\rho U_r^2 A} \tag{9}$$

$$C_D = \frac{D}{\frac{1}{2}\rho U_r^2 A} \tag{10}$$

where ρ is the fluid density, U_r is the relative velocity of the incoming flow, and A is the frontal area (the projection of the blade on a plane normal to the flow direction).

Figure 2.2 illustrates the lift and drag forces with respect to the relative velocity(U_r). It also reveals the torque and thrust acting tangentially and normally to the blade section rotational plane, respectively. The torque and thrust are linked to the hydrodynamic forces (lift and drag) by Equations 11 and 12, respectively.

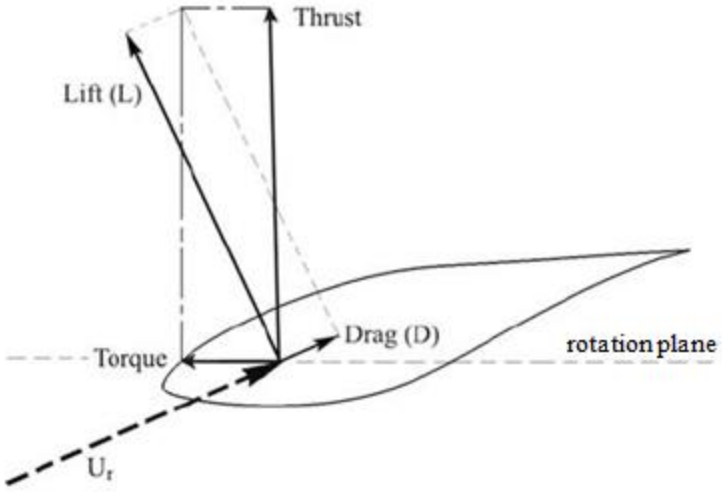

Figure 2.2. Load on a typical hydrofoil [37]

$$\text{Torque force} = L\sin\phi - D\cos\phi \tag{11}$$

$$\text{Thrust force} = L\cos\phi + D\sin\phi \tag{12}$$

Power (P) and power coefficient (C_p): The power generated from a turbine is calculated from data (torque and rotational speed) that is acquired experimentally. This power is defined as the torque multiplied by the angular velocity and is given by

$$P = T.\omega \tag{13}$$

where T is the torque magnitude (N.m), and ω is the rotational speed (rad/sec). An HAHkT's performance is determined, primarily, by the power coefficient (C_p). This coefficient is defined as the ratio of the output power to the available kinetic power in the flowing water that passes the turbine swept area. It is given by

$$C_p = \frac{P}{\frac{1}{2}\rho U^3 A} \tag{14}$$

where P is the power output of the turbine, ρ is the water density, U is the free stream velocity, and A is the swept area of the turbine. Both the torque sensor and the clutch are mounted onto the system output's vertical shaft (beyond the transmission shafts and the bevel gears). Thus, the power coefficient in this research reflects the system overall efficiency.

Cut-in speed: The cut-in speed is defined as the flow velocity at which the turbine first begins to rotate and generate power.

2.1.2. Experiment Variables. There are two experimental design parameters that were investigated in the study. These parameters are specific to the multi-turbine system.

Rotors relative installation angle (∅): The rotors relative installation angle is defined as the angle between the blades from two consecutive rotors. This angle was varied to investigate its effect on the multi-turbine performance (see Figure 3.18 a).

The axial distance between rotors (x): The axial distance between turbine system's rotors is defined as the axial distance between two consecutive rotors' planes of rotation; it was varied as a factor of the rotor's diameter (D). This parameter was used for two purposes: 1) to investigate its effect on the turbine system performance, and 2) to examine the wake characteristics at different axial distances behind the rotor. Refer to Figures 3.18 b and 3.19 for illustration of this axial distance (x).

2.2. STALL PHENOMENON

The flow dynamic principle of hydrokinetic turbines is similar to the flow over a hydrofoil. In turbines, incoming flow with a given AoA (α) generates lift force to rotate the rotor. For a particular blade section along the blade span, when α has a moderate value, C_L increases linearly with α and the flow moves softly and attached over most of the hydrofoil. The C_L continues to increase with increasing α until a certain value is reached. The C_L reaches its maximum value at this critical value of α. If the α is increased beyond this limit, the hydrofoil is said to stall, and the C_L begins to decrease. Stalling occurs because the flow tends to separate from the hydrofoil's upper surface. The fluid that flows over this upper side accelerates as it passes the leading edge, close to the

stagnation point. This flow acceleration causes the pressure to drop along this side. The pressure gradient on the lower side is smaller than that on the upper side because the curvature of the wall is smaller than the front leading edge. According to the Kutta condition, the pressure at the trailing edge (at the end upper and lower sides of the hydrofoil) must be equalized. Therefore, to satisfy this condition, the pressure must increase from a minimum value at somewhere on the upper side to a higher value at the trailing edge. This change in pressure gradient from, ($\frac{\partial p}{\partial x} < 0$) to ($\frac{\partial p}{\partial x} > 0$), creates an inverse flow and causes the axial velocity profile to have an S-shape. This shape may lead to a separation in the flow particularly when the angle of attack (α) is high [38].

The flow separation may be delayed under the effect of both centrifugal forces along the blade span and Coriolis forces along the blade chord. This phenomenon is known as dynamic stall. It is beneficial to the rotating turbine because the flow separation is either delayed or shifted to a point closer to the trailing edge. This shift keeps the pressure low over most of the upper suction side. Consequently, the delay in flow separation allows the blade to gain higher lift values, generating higher torque and thus higher power. Another parameter that affects the stall is the hydrofoil geometry; the hydrofoils with a high curvature around the leading edge tend to stall more suddenly than the hydrofoils with a lower curvature [38].

2.3. WAKE AND VELOCITY DEFICIT

The wake is produced when the flow stream's momentum decreases. This decrease in momentum is caused by a turbine when extracting the kinetic energy from the passing flow. The fluid that flows across the turbine swept area applies a torque on the turbine rotor. A reacting equal and opposite torque is imposed upon the flow by the turbine blades. Subsequently, in the downstream regions, besides the reduced axial velocity component, the flow also has a tangential velocity component that is opposite in direction to that of the rotor blades [41]. Understanding the turbulent wake plays an important role in optimizing the turbine efficiency and the turbines arrangement in either the water farm turbines or coaxial multi-turbine systems [42].

The wake, which is downstream from the turbine, can be classified into two regions. This classification of wake is based on the proximity to the rotor and the influence of the rotor on its characteristics. These two regions are the near wake and the far wake regions. The near wake region lies immediately behind the rotor and expands downstream to a distance of approximately one rotor diameter length. Here, the wake expansion is driven by the momentum extraction from the stream while maintaining the conservation of mass. The rotor influence is obvious on the near wake (e.g., the rotor's blade number and the blade hydrodynamic characteristics). These characteristics, including the stalled flow, the effect of 3-D flow and the tip vortices, play a key role in the near wake structure. The near wake is typically studied to better understand not only the turbine's performance but also the physics behind power extraction [43-45].

The far wake region is located beyond the near wake; the two regions are separated by the transient wake region. The initial conditions in far wake region are formed by the previous near wake region. Here, the wake model is more important than the actual rotor model because the emphasis is on the mutual influence of the turbines when they are arranged into arrays (e.g., farm turbines). A shear layer surrounds the wake and separates the slow flow inside the wake from the fast flow outside it. This shear layer has a thickness that increases as it moves downstream. The thrust on the rotor increases as the turbine load increases. This increase in thrust is associated with a simultaneous increase in flow impedance, causing the wake to slow down. As a result, a larger shear is formed due to the increased difference between flow velocities inside and outside the wake. At very high rotor loading, a large amount of kinetic energy is converted to a large scale turbulent motion. As a result, the turbulent wake state is formed. The mixing of lower velocity fluid inside the wake with the higher velocity fluid outside the wake allows the momentum to transfer. This in turn results in expansion of the wake and reduction of the velocity deficit [43, 44, 46].

In summary, it is important to understand the effects a turbine has on the flow for better improving this turbine's performance. Furthermore, understanding both the evolution and dissipation of wake is essential to optimizing the arrangement of turbines in an array [43].

2.4. OBJECTIVES

Hydrokinetic turbines convert the kinetic energy in flowing water to mechanical power by reducing the flow velocity. A theoretical limit called Betz limit is the ceiling of the kinetic energy that can be extracted by axial turbine from the flow. Simply, Betz limit is the highest energy can be captured by the axial turbine which cannot exceed 59.3% of the kinetic energy exists in the flow. The ratio 59.3% is the theoretical power coefficient for a single and unducted actuator disc. The Betz limit is often used as a reference for estimating the maximum efficiency of these types of turbines [8, 27]. Different measures can, however, be taken to help make HAHkTs approach or even exceeded this limit. For example, increase the generated power by enhancing the water velocity through shrouding the turbine with a duct. The turbine performance can also be improved by optimizing several hydrodynamic parameters (e.g., pitch angle, solidity, and number of blades).

This work was conducted as an attempt to improve the efficiency of small HAHkTs that harness kinetic energy from river stream. Several experiments were performed in a water tunnel to investigate small-scale HAHkT models with various configurations. The power output of these different turbine configurations was determined by measuring both the output torque and the rotational speed.

Four set of experiments were completed to fulfill this study. The first set of experiments provided insight into the operating characteristics of a 3- blade single turbine. Here, the effect of pitch angle (θ, hence, AoA), the tip speed ratio (TSR), the applied load, and the flow velocity (U_∞) on the generated power were each analyzed. This analysis helped clarify how these parameters interact to affect the turbine's performance.

Traditional HAHKTs suffer from low-efficiency as a result of their non-optimized rotor configuration. Various hydrodynamic variables control this turbine's performance (e.g. blade number, solidity, swept area, and rotors configuration). The output power increased as the solidity of the rotor increased. Increasing the solidity beyond the optimum limit, however, causes a decline in the generated power [42] because the flow across the rotor's swept area decreases (see Figure 2.3). (Solidity increased for specific

rotor diameter by adding more blades or increasing blades chord.) The solidity can be maintained with increasing the blade number or chord width by increasing rotor's diameter. This also increases the rotor's swept area [See (14, 15)]. The rotor's swept also influences the generated power. Nevertheless, the swept area is a function of the rotor's diameter, which is limited by the river's depth. A novel multi-turbine system (two or three rotors mounted coaxially to the same shaft) was introduced in this study to avoid the high solidity resulted from adding blades to the same rotor. Moreover, to overcome the rotor's swept area limitations (more rotors, technically, increases the swept area). The results were promising; adding rotors allowed the system to cut-in at a lower flow velocity than did the single turbine systems.

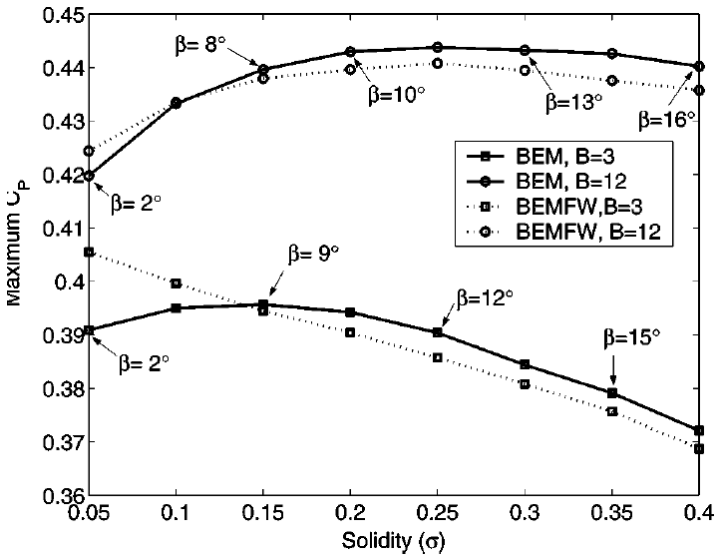

Figure 2.3. Maximum C_p versus solidity for constant chord, untwisted blades. Pitch angle θ= 0^o-20^o [42]

A duct reducer was used in the third set of experiments. This duct was proposed to investigate the influence of a duct reducer on both a 3-blade single turbine's performance and a multi-turbine system's performance. It was also proposed to compare their responses after using this duct. No attempt was made to improve the duct's performance.

The fourth and final set of experiments was conducted to visualize the downstream flow and acquire a transient 2D contour of the flow velocity, hence, related flow characteristics in the wake regions. Both 3- and 6-blade single turbines were utilized. These turbines were exposed to a fixed stream velocity ($0.594\ \mathrm{m/s}$) and loaded with a fixed torque ($0.015\ \mathrm{N.m}$). The flow was then visualized at different downstream axial location to determine the effect of blade number (or solidity) and axial downstream distance on flow wake recovery. The effect of increasing flow velocity on the wake structure was also inspected at fixed axial position (4D) behind the 3-blade turbine. A study of the near wake provided details on the turbine's energy loss at an ambient flow region. This study also allowed for an analysis of the turbine's mutual influence when are arranged into arrays.

2.5. PREVIOUS STUDIES ON THE HAHkTs

During the last decade, several experiments and numerical simulations had been performed to investigate the hydrokinetic and marine current turbines [37, 47-49]. This was to establish better knowledge about flow dynamic and the effect of various hydrodynamic variables on the turbine output. However, few investigations have focused on the effect of pitch angle (and thusAoA), solidity, and blade number on the performance of small HAHkTs.

2.5.1. Angle of Attack and Pitch Angle. Thumathae and Chitsomboon [37] performed a computational fluid dynamics numerical simulation (CFD) of horizontal axis wind turbine with untwisted blades to define the optimal angle of attack that generates higher power. They found that an optimal AoA neighbors the maximum lift point and the lift to drag ratio has insignificant effect on the optimum AoA when a section at 80% of the blade span is used as design bas. Batten et al. [50, 51] conducted experiments in a cavitation tunnel and performed a numerical method using blade element momentum (BEM) theory. Their results illustrate how both pitch angle and changes in the camber affect the delay stall performance and cavitation inception for marine current turbines. They also found that the power coefficient increases as the pitch angle decreases. Similar observation was stated in [52] and more others.

2.5.2. Number of Blades and Solidity. A number of studies [21, 42, 53, 54] have been conducted, either experimentally or numerically, to investigate the effect of solidity and blade number on the performance of wind turbines and water turbines. Various studies have been performed at Clarkson University to investigate the effects of solidity, blade number, and pitch angle on the performance of small horizontal axis wind turbines (HAWTs). The results from these studies indicate that aerodynamic gains occurred when both the solidity and the number of blades increased. The pitch angle controlled the TSR range of operation; decreasing the pitch angle increased the operational range of the optimum TSR [42, 54]. Rector et al. [54] experimentally investigated the influence of solidity, the number of blades, and the pitch angle on an HAWT's performance. They found that the cut-in speed decreased when either the solidity or the number of blades increased. This decrease in cut-in flow speed is attributed to the increase in starting torque [54] (similar observation was found in this research for HAHkTs). They also suggested that the TSR decreased dramatically at a maximum C_p when the pitch angle increased. The maximum C_p increased, however, when the pitch angle decreased, improving efficiency

Kolekar et al. [31] noted that the optimum TSR is located between two extremes. A high TSR decreases the AoA and reduces the lift. In contrast, a low TSR increases the AoA, which stalls turbine. This finding has been confirmed in several different studies that examined various water and wind turbines [42, 53, 54].

Duquette and Visser [42] used a simple BEM theory, with different correction factors, to examine HAWT with untwisted blades. They found that increasing the number of blades at a given solidity will always increase the maximum C_p. The optimum TSR (at which the maximum C_p is reached) was strongly affected by solidity. Changing the number of blades with maintaining the solidity, however, had a little influence on optimum TSR. Moreover, increasing solidity slightly narrowed the range of TSR operation.

Mukherji et al. [21] used a 3D numerical model of HAHkT that solved in CFD analysis. They found that an increased solidity enhanced turbine performance which is similar to [42]. Increasing the number of blades at a given solidity, however, showed that

the 3-blade turbine is the optimum compared to 2-and 4-blade turbine. This is unlike to what was found by Duquette and Visser [42] for wind turbine.

2.5.3. Duct Reducer and Diffuser. A number of researchers have investigated the use of ducts in attempt to improve the turbine hydrodynamic efficiency. Most of these studies focused on the wind turbines; few studies examined the use of ducts with water turbines. It has been strongly argued that, even though some improvement of wind turbine is achieved when using a duct under ideal condition, the additional cost of establishing a diffuser (duct) will far surpass the advantages. The reason is owing to the added weight and drag to be supported by the turbine tower. Unlike the wind turbines, the water turbines duct weight is of less concern due to buoyant forces [13, 30].

Ponta et al. [55, 56] used a series of channel models to investigate a vertical axis water turbine's performance. These channels were modeled to have a nozzle (to accelerate the flow), a straight channel (to host the rotor), and a diffusor (to adjust the flow to the ambient). The model's initial design was based on results obtained from a theoretical model of the internal flow. They found that the percentage flow speed increment increased and the power peak shifted toward lower flow velocities when an optimized duct was used. They also found that the flow in their channel was steadier and less dependent on the river current's speed.

Gilbert and Foreman [57] performed a number of experiments with wind tunnel models. They found that a ducted turbine generated power 4.25 times more than if it was unducted. They suggested that slots to be used to permit the high velocity flowing outside the diffuser to flow inward for boundary layer control. Their diffuser, short with a wide angle, is thought to be more economical than long diffusers.

Setoguchi et al. [58] noted that the outside body geometry of a diffuser plays a key role in improving the diffuser's performance. They used a three part circular diffuser (a nozzle at the front, a straight tube in the middle, and a diffuser at the end) with a brim (flange) around its exit edge. They found that a diffuser with a straight outside surface had better performance than did base and bulge type diffusers.

Nasution and Purwanto [59] investigated the effect of a diffuser's interior surface shape on its performance. They used a diffuser similar to that used by Setoguchi [58] (a

diffuser with three parts, a flat outside surface, but no flange at the exit). Two conical diffuser models were set, one with a flat inner surface and another with a curved inner surface. The study confirmed that, with using the diffuser with curved interior surface, a local velocity augmentation can achieve 65.5% compared to the diffuser with flat interior surface. They noted that the reason of this high velocity augmentation was caused by the higher formation of turbulence behind the diffuser.

2.5.4. Wake. The Final part of this study addressed the characterization of an HAHkT's wake. Understanding the effects turbines have on flow is important to understanding how these turbines may adjust both the performance of and the loading experienced by turbines downstream [43]. Numerous studies have used several techniques (e.g., field observations, laboratory scale experiments, and numerical simulations.) to investigate the wake created by wind and water turbines.

Chamorro et al. [45] performed a 3D flow visualization to investigate the near wake region behind a 3-blade axial-flow turbine. They found that the wake expansion is proportional to the streamwise distance to the power of one-third, within the first rotor diameter. The tangential velocity was found small near the turbine tip as a result of the surrounding flow. Therefore, this tangential velocity can be neglected at this region. The tangential velocity at a particular radial position decayed as the streamwise distance increased. The radial velocity was higher near the rotor tip and decreased toward the hub center due to the rotor symmetry.

Bahaj et al. [43] investigated the far wake region behind small-scale disk models in a 21 m tiling flume. These models were set to have different porosity levels that yielded various thrust forces. Bahaj et al. [43] suggested that the far wake region characteristics generated by the disc are similar to that generated be the full scale actual rotor. They showed the constraint effect by the free surface on the wake expansion. They also found that the wake centerline was located below the disc centerline due to the combination of shear layers and bounding free surface. The velocity deficit was reported to decrease with the increase of downstream distance. Finally, the wake velocity was shown to be a function of the free stream velocity, but the velocity deficit displayed general recovery trend.

Xiao et al. [60] used single solid disks, porous disks, and an array of four porous disks to investigate the near wake region. They found that the porous disk decreased both the velocity deficit and the rate of velocity recovery (with streamwise distance) more than the solid disk did. The array reduced the wake velocity deficit. Nevertheless, it reduced the rate of the wake velocity recovery only slightly.

Mukherji et al. [21] used 3D numerical simulation (CFD) to investigate the wake behind a HAHkT. In this study, they analyzed the three velocity components ($U_x, U_y,$ and U_z) present within the wake at different downstream axial locations. The wake expanded as it travelled downstream. However, the axial velocity deficit decreased rapidly after two rotor lengths downstream. The other normal velocity components had a smaller magnitude than did the axial component, indicating that the axial velocity distribution had the greatest effect on power extraction. Similar observations were obtained in this research.

3. METHODOLOGY

3.1. TECHNIQUES UTILIZED

3.1.1. Water Tunnel. A water tunnel in the water tunnel lab, located within Toomey Hall at Missouri University of Science &Technology (M S&T) was used to conduct all hydrokinetic turbine system tests. This water tunnel was comprised of non-corrosive materials supported by a painted steel framework. The interior side of the facility had exceptionally smooth finished surfaces.

The test section of the water tunnel was 0.381 meters (15 inches) wide, 0.508 meters (20 inches) deep, and 1.524 meters (60 inches) long. The test section surfaces were made principally of tempered glass to allow maximum viewing of the tested model from five sides. The test section had one open surface in the top. It also had other four glass sides allowed the water tunnel to be used with Particle Image Velocimetry system (PIV).

The water tunnel had an overall volumetric capacity of approximately 1000 gallons. The maximum water velocity that could be reached in the test section was approximately 0.9565 m/s (36.657 inch/sec), according to the manufacturer's first set of calibrations. A speed controller was used to vary the pump frequency (over 9 pump engine frequencies in the range between 2.5 to 40 Hertz (Hz)) so that the flow speed in the test section could be controlled. A flow meter sensor was used to measure the flow speed through the test section. A Clamped Cubic Spline Polynomial was then used to plot the data. This information provided flow velocity values within the test section for the entire range of frequencies. An illustration of the facility used in this study is given in Figure 3.1. Pump engine frequencies and their corresponding flow speeds are given in Table 3.1 and Figure 3.2, respectively. A PIV system was used to calibrate the water tunnel because the sensors could either deviate or fail over time. All of the experiments were conducted according to the last calibration performed.

Figure 3.1. Water tunnel facility

Table 3.1. Pump frequencies vs. test section flow velocity

Hz	m/sec
0	0
2.5	0.056921
5	0.11237
10	0.222123
15	0.31181
20	0.422351
25	0.520294
30	0.635889
35	0.753212
40	0.956488

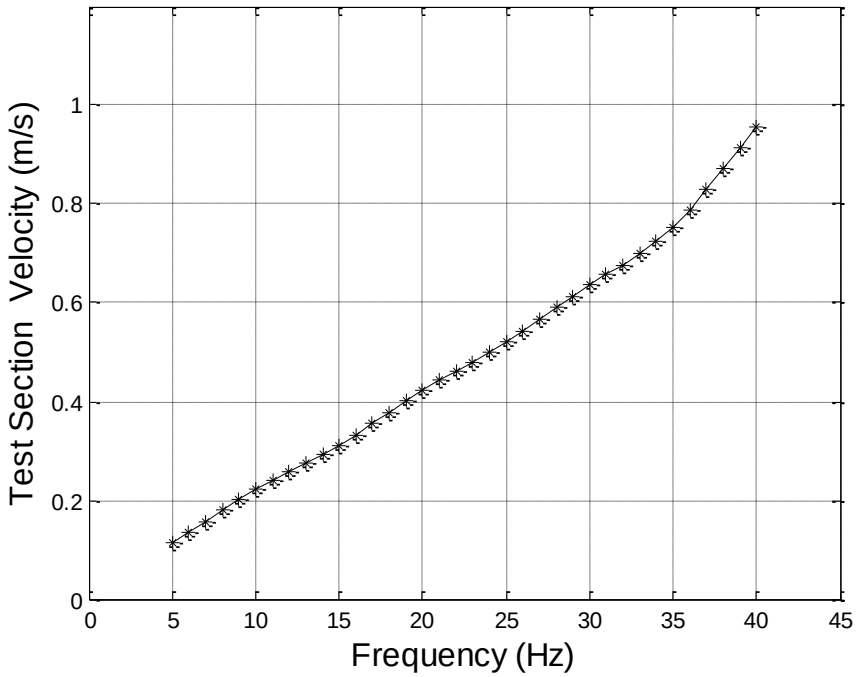

Figure 3.2. Pump frequencies vs. test section flow velocity

3.1.2. Horizontal Axis Hydrokinetic Composite Turbine (HAHkCT). The turbines used in this experiment were designed to be lightweight in an effort to reduce the friction losses. The blades were made from a composite material (prepreg Cycom 5320), and the hubs and the shafts were made from aluminum.

3.1.2.1 Blade design and manufacturing. The composite blades (intended to be used for both a three and a six-blade HAHkCT) were untwisted and had a fixed chord length. A mold (ULTEM 9085) obtained from Stratasys was used to manufacture the blades (see Figure 3.3).

The twisted blades have been confirmed to have higher performance compared to their counterparts (the untwisted blades). The reason is that, twisted blades have full utilization of their area to produce lift at low drag while providing better starting torque. However, untwisted blades are beneficial for small and medium turbines owing to the ease in manufacturing, thus low cost [37].

Figure 3.3 Blade mold (upper/lower half mold)

Out of autoclave process (AOO) was utilized to manufacture the turbine blades. The process begins by placing the upper and lower parts of the mold on an aluminum plate mold. For each part of the mold, three layers of carbon/epoxy prepreg were cut to dimension and laid up in the order of 0º/90º/0º. (These angles were referenced to the mold's longitudinal direction.) Sufficient care was taken to ensure that no air was trapped between the layers. Next, each set of three layers was placed between two layers of fluorinated ethylene propylene (FEP). The sets were then laid down onto the upper and lower parts of the mold (ULTEM 9085). The FEP was used so that the manufactured blade parts would be easy to remove after curing was complete. A layer of breather was applied to cover the two parts of the mold. An outlet air valve was placed on the breather, and the entire aluminum mold was vacuum bagged (see Figure 3.4). Vacuum of 760 millimeters (28 inches) of Hg was applied, and the sample was put in an oven and cured as recommended by the manufacturer's cure cycle.

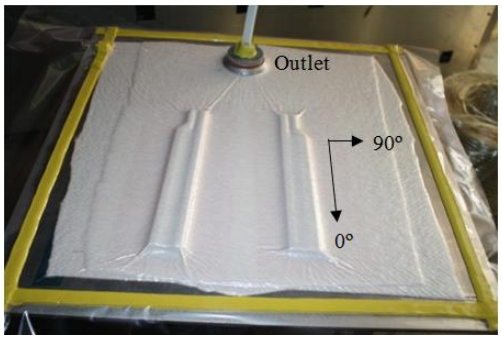

Figure 3.4 The manufacturing process used to manufscture composite blades

A steel rod was fitted to each composite blade's root to serve as reinforcement. This steel rod was used so that the blades could operate at a high flow speed without experiencing root failure as a result of high thrust forces. Finally, the cured upper and lower composite blade halves were matched together and glued. Figure 3.5 is an image of manufactured composite blades that need additional cutting and polishing before application.

Figure 3.5 Manufactured composite blades

The blade's span length was cut down to 86.36 millimeters (3.4 inches, without the root) so that the turbine could be fitted inside the duct rear pipe. The blades' width was 16.76 millimeters (0.66 inches). It had a constant cross-section (Eppler 395), without a twist, so that the design parameters could be quantified more accurately [35].

3.1.2.2 Hydrokinetic composite turbine hubs. The three-blade horizontal axis hydrokinetic composite turbines (HAHkCTs) that was used in both single and multi-turbine systems (coaxial turbine system) had a hub with diameter and length of 25.4 millimeters (1 inch). The hub was designed to have two parts. These parts clamped the three blades (as illustrated in Figure 3.6 a) so that the blade's pitch angle was adjustable.

The six-blade HAHkCT had a hub with a diameter of 31.74 millimeters (1.25 inch) and a length of 23.5 millimeters (0.9252 inch). This hub was designed to be somewhat different from those previously used; it did not utilize two parts to clamp the blade roots. Instead, a set of setscrews was placed at the bottom of the hub, fixing the blades' roots so that they could not rotate (see Figure 3.6 b).

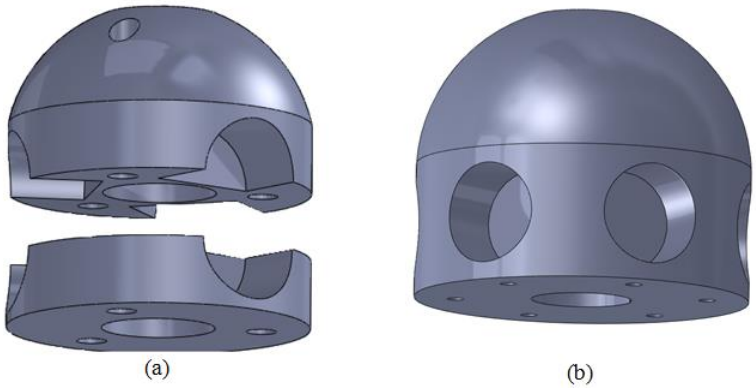

Figure 3.6. The (a) three- and (b) six-blade HAHkCT hubs utilized in this study

3.1.3. Experimental Data Acquisition Devices. The experiment outputs were the torque and rotational speed which were required to calculate the harvested power by the turbine system. The two sensor components that used to acquire the data are discussed in detail in the next two sections.

3.1.3.1 Torque sensor and clutch. A FUTEK reaction torque sensor (maximum torque 50 in-oz, 0.353 N.m) was used to measure the system's torque output. The torque sensor was aligned with and attached at its upper end by a magnetic particle clutch C2 (maximum torque 32 in-oz, 0.226 N.m). The lower end was rigidly fixed to the plate form of the torque sensor's assembly. The clutch shaft was coupled through a universal joint to the top end of the turbine system vertical shaft (the turbine system output shaft, see Figure 3.7).

The torque sensor was then wired to the FUTEK USB210 device (which works as a data acquisition device.) This device continually received and stored torque data signals. It then transferred these signals to a LabVIEW interface program that was adapted from the FUTEK USB accompanied code. The code was modified so that the data did not need to be exported to excel sheets for calculation; moreover, to allow the user of monitoring the average torque instantly. The code was modified by adding a waveform chart and waveform chart history terminal that save the processed torque sensor signals over time. The waveform chart history data was averaged instantaneously

through a mean terminal. The average output then was updated and presented continuously by an interface numerical indicator.

A power supply with controllable voltage and current was connected to the clutch. As a result, the applied load on the turbine could be adjusted and thus both the turbine torque and the rotational speed could be controlled. Figure 3.8 is an illustration of the torque sensor components.

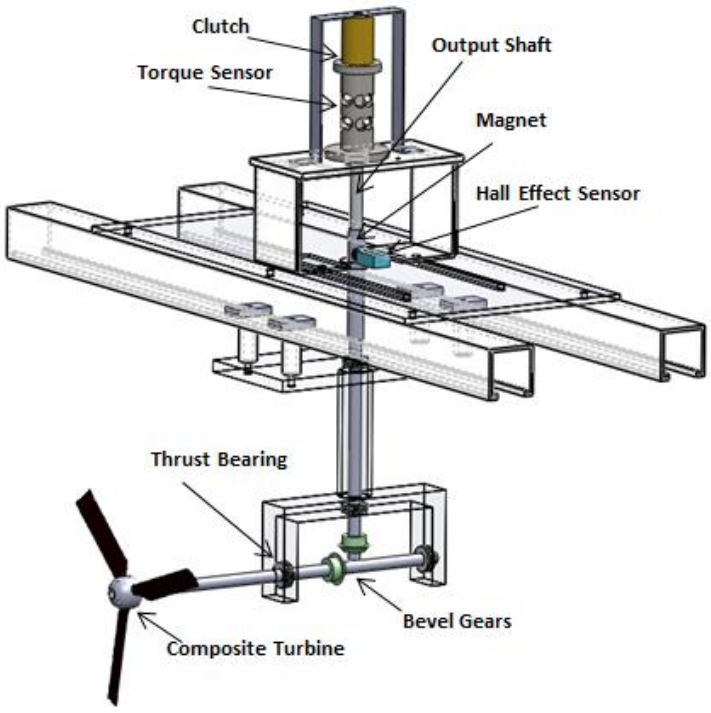

Figure 3.7. Torque sensor assembly setup

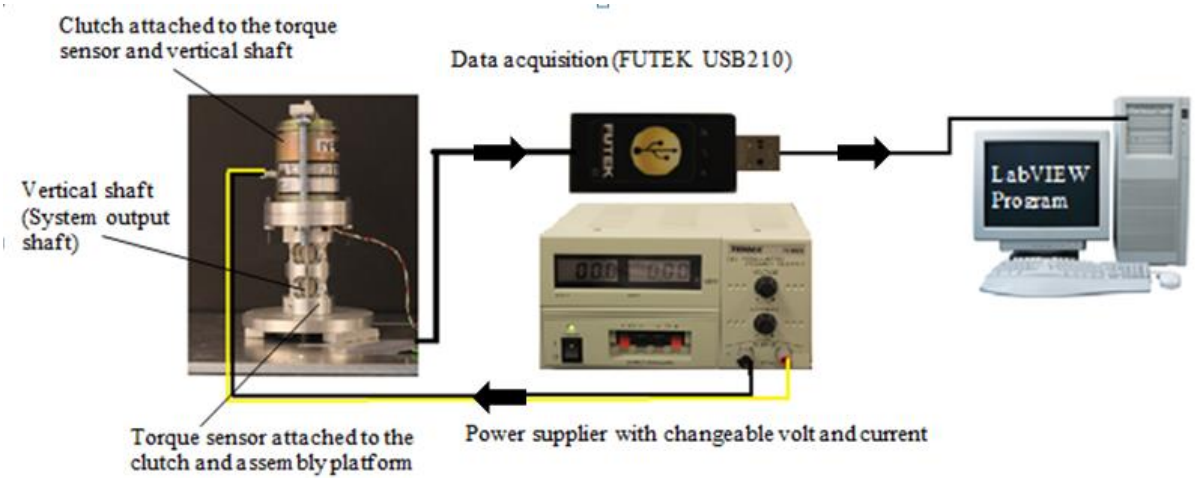

Figure 3.8. Torque sensor components

3.1.3.2 Time-averaged RPM sensor. The turbulent flow effects, combined with an imperfect alignment in the turbine system's components, produced unequal friction over the turbine cycle. This friction created small fluctuations in the rotational speed. A typical laser tachometer is inadequate because it measures the instantaneous RPM, not the average RPM of the rotor over time. Thus, a Time-Average RPM sensor was needed to ensure the accuracy of collected RPM data and the synchronization with torque sensor collected data over definite period of detecting time. As a result, precise and reliable calculated power output will be attained.

The sensor used in this study was adapted form information on a sensor that was originally operated as a casual tachometer [61]. The Time-Average RPM sensor was comprised of a Hall Effect sensor, an earth magnet with a diameter of 0.1875 inches (4.7625 millimeters), a breadboard, a data acquisition device (NI myDAQ), and a LabVIEW interface (see Figure 3.10). The Hall Effect sensor was wired and embedded in a plastic case. It was then partially glued with hot glue to not only protect it but also ensure firm joints between the sensor ports and the wires. Once complete, the sensor was mounted onto the torque sensor assembly platform, 3 millimeters from the vertical shaft (the turbine system output shaft, to which the magnet was attached). Each time the magnet passed the Hall Effect sensor, the sensor was triggered to produce electrical signals. These signals then magnified throughout the breadboard's electrical circle. The

data acquisition device received, processed, and controlled these magnified signals. It then transported them (for processing and monitoring) to the LabVIEW interface program. Figure 3.9 depicts how the Hall Effect sensor and data acquisition were wired through the electrical circuit. Refer to Appendix A for the LabVIEW code and interface used.

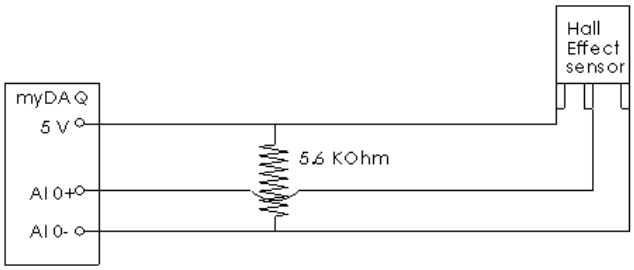

Figure 3.9 The electrical circle that connected the Hall Effect sensor to myDAQ

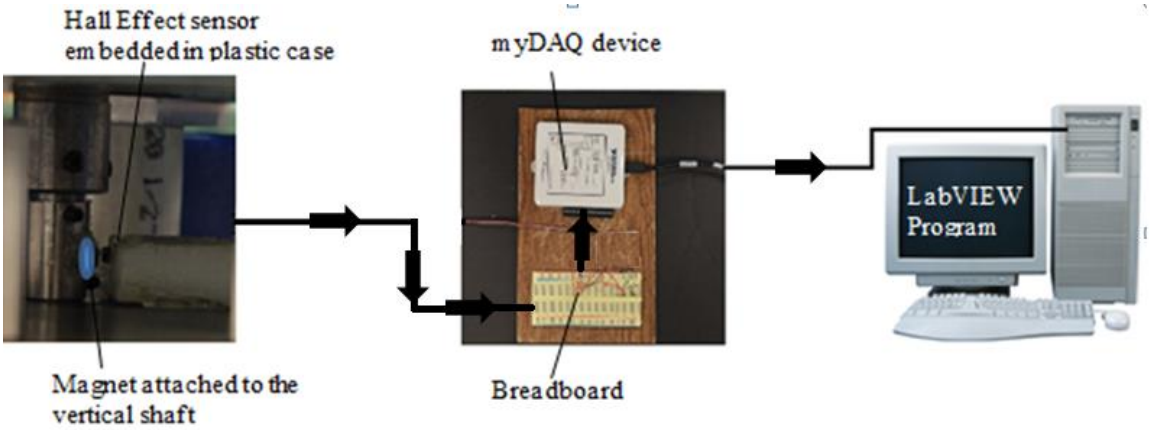

Figure 3.10 Average-Time RPM sensor components

3.1.4. Duct Reducer. A duct reducer was used to enhance the flow through the turbine rotor thus increasing the generated power. The duct, illustrated in Figure 3.11, was comprised of LaserLock galvanized metal that had a thickness of 1.27 millimeters (0.05 inches). The entire duct consisted of two parts. The front part (the reducer) had a length of 0.1905 meters (7.5 inches), an inlet diameter of 0.3048 meters (12 inches), and

an outlet diameter of 0.2286 meters (9 inches). The rear part (the pipe), which housed the turbine system, had a length of 0.9017 meters (35.5 inches) and a diameter of 0.2286 meters (9 inches.) The ratio of reduction area was chosen to be 12 to 9. This ratio guaranteed that the blockage is less than 20% of the water tunnel flow cross-section area to avoid high turbulent flow effects. The two parts were joined by a clamp, and the entire assembly was hung on the water tunnel's shoulders.

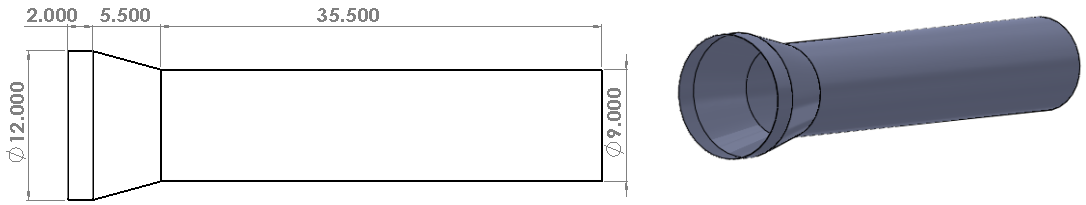

Figure 3.11 The duct reducer (12 to 9 inches) joined to the pipe

3.1.5. Particle Image Velocimetry (PIV). A PIV system was used in this research to calibrate the water tunnel flow speed. It was also used to allow for a visualization of the downstream flow and thus acquire a transient 2D contour of the flow velocity inside the wake. Understanding the wake structure gives a good indicator of the kinetic energy that captured by the rotor [46]. Moreover, studying the development of the wake in the downstream flow regions aids in setting the multi-turbine system's rotors at appropriate distances. As a result, the efficiency of the system increased. The PIV system's components are detailed in Table 3.2. Figure 3.12 is a schematic diagram of a hydrokinetic turbine placed in a free water flow, in the test section of the water tunnel. Figure 3.12 also shows the setting of PIV system components.

Table 3.2. Functional description of a PIV system's primary components.

Analysis • Insight 4G Software • Computer and all the peripherals installed in the computer.	Analyzes PIV images and computes flow field parameters.
Synchronizer • Model 610036 LASERPULES Synchronizer	Timing electronics for all of the components in a PIV image system. It controls the laser, camera, and image shifter so that each component operates in the correct sequence.
Laser • Nd: YAG Lasers • Lightsheet Optics • Breadboard	Provides the illumination for the flow field.
Image capture • Video PIV System • Film Capture 1. This includes Model 630059 POWERVIEW Camera System which consists of: 2. 1 POWERVIEW™ Plus 4MP Camera 3. 1 Accessory Kit POWERVIEW 4M plus 4. 1 Lens 28-mm F/2.8 Af Nikkor Lens	The camera and its components are used to digitize the image. With video cameras a frame grabber is used to digitize an image. With film-based systems a slide scanner is used to digitize the film.

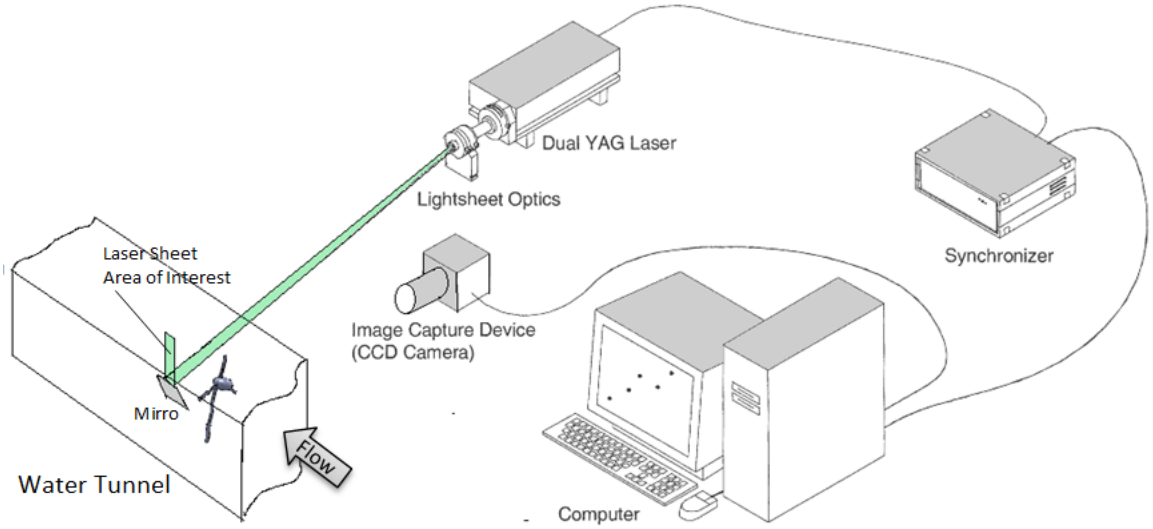

Figure 3.12. Schematic of an experiment that utilizes a PIV system

3.2. EXPERIMENTAL SETUP

The HAHkCT system was comprised of either 3- or 6-blade rotors, as well as transmission shafts. The mechanical power generated by the turbine system's rotors was transmitted to both the torque and the RPM sensors via two coupled horizontal shafts and one vertical shaft. One of the horizontal shafts (the main shaft) that held all of the rotors had length of 1.27 meters (50 inches). Its diameter had small tolerance to mate, at one end, a fixed (stationary) hub that has inner diameter of 9.525 millimeter (0.375 inches). This hub was attached firmly to a vertical rod that was bolted to a transversal plate. The bolt had long thread to facilitate a vertical alignment between this hub and the torque sensor's assembly horizontal shaft. A number of two C clamps were used to attach the transversal plate to the water tunnel test section's shoulders, near the test section's inlet (the upstream region.) A universal joint was used to couple the other end of the main horizontal shaft to the torque sensor's assembly horizontal shaft and thus reduce the effects of misalignment. Thrust bearings were mounted to the fixed hub and the torque assembly. Setscrews were used to fix collars around the horizontal shafts' ends. These collars prevent the thrust bearings and shafts from moving under the flow thrust force. They also transfer the thrust force acting on the rotors to the thrust bearings.

Torque assembly was attached (by means of C clamps) to the water tunnel test section's shoulders near the test section's exit (the downstream region.) Three setscrews were used to mount each turbine (the turbines had inner diameters similar to that of the fixed hubs) to the main shaft. The three setscrews were equally distributed around each rotor hub circumference to prevent the rotors from slipping under flow forces and to ensure centrality of the rotor hub with the shaft.

The duct reducer also had two transversal plates. These plates were used to hang the duct reducer from the water tunnel test section's shoulders (between the front fixed hub and the torque sensor assembly). Figure 3.13 is a schematic of all of the assemblies, together, placed on the water tunnel's shoulders.

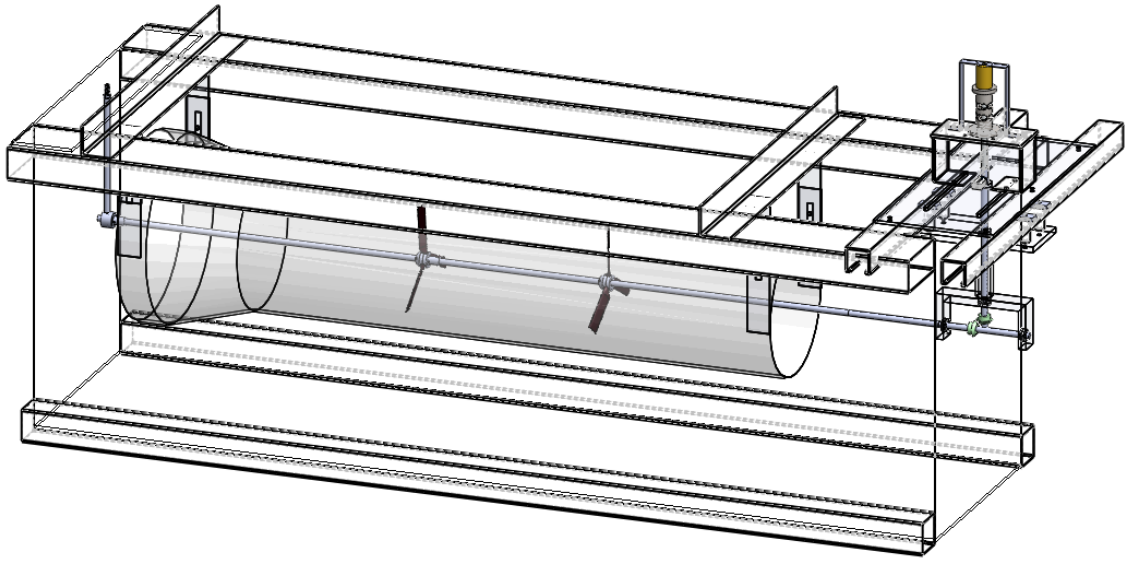

Figure 3.13. Ducted turbine system's assembly

3.3. EXPERIMENTAL CALIBRATION

The sensors were calibrated before the tests were begun to ensure accurate and reliable experimental results.

3.3.1. Water Tunnel Calibration. The water tunnel was calibrated to validate the relationship between the water tunnel flow velocity and pump engine frequencies originally submitted by the water tunnel's manufacturer (ROLLING HILLS RESEARCH CORPORATION.) PIV was used to monitor the flow at the middle of the water tunnel test section and thus acquire instant 2D velocity measurements.

The first step in experiment involved connecting the PIV system components (as indicated by the manual). A digital camera (with a CCD chip) was then leveled and adjusted to point toward the test section, covering the area of interest. Seeding particles (with a mean diameter of 9-13μm and a relative density of 1100 kg/m3) were dispersed in the water tunnel, and the laser (with a cylindrical lens) was used to shoot a laser sheet at a mirror (placed earlier) at the bottom of the test section. This mirror reflected the laser sheet upward, covering the flow region of interest (region was parallel to the test section's sides and perpendicular to its bottom.)

Initial PIV calibration was required to calculate the velocity vector magnitude in metric units instead of pixels. A scale of 1.27 meters (50 inches) was located vertically along and just behind the laser sheet. Both the aperture and the focus of the camera's lens were adjusted to obtain a clear view of the seeding particles. A calibration image was taken once these adjustments were completed. PIV software (Insight 4G) was used to mask the area of interest and calculate the millimeters per pixel value.

The PIV hardware components were specified and set to appropriate values, before the images could be captured and the flow speed could be analyzed according to the application used. The exposer was set to a synchronized mode so that the synchronizer's trigger could control the camera shutter and the laser pulsing. All of the component's timings were adjusted so that, when the synchronizer triggered the system, the laser was pulsed between the camera's frames. The capture was set to sequence so that the number of images required for the experiment could be specified. The laser power was set to the highest level so that clear view of the seeding particles could be obtained.

The frame mode was set to straddle so the camera could acquire two consecutive single-exposure images. As a result, the number of frames the camera could capture when

triggered by the synchronizer could be defined. The PIV used these frames to calculate the seeding particles' velocities based on the particle spatial shift in the images and the corresponding time between them. It should be noted that, the PIV system was matched to the flow velocity by adjusting the time for pulse separation based on the flow velocity. This was achieved by adjusting the particle image displacement to be less than one quarter of the 64-pixel spot. This adjustment specification allowed for better tracing of the flowing particles.

Finally, for each water tunnel velocity, a number of 100 optical images were taken to capture the area of interest. (For the wake investigations about 500 images are required due to the turbulent flow effects).The preprocessor, processor, and post-processor were each set to an appropriate setup. The captured images were processed first and then imported to Tecplot 360 software. This software calculated the average flow speed for every frequency obtained.

The water tunnel calibration test was conducted twice. The averaged results, with their corresponding pump frequencies, are listed in Table 3.3. The previous Clamped Cubic Spline Polynomial was used again so that the entire range of flow velocities corresponding to every one increment of pump frequency could be obtained. Figure 3.14 illustrates the relationship between the stream velocities and the pump frequencies for both the manufacturer's data and the PIV data. The curve in Figure 3.14 illustrates all the range of data collected, including that taken from the Clamped Cubic Spline Polynomial.

Table 3.3. Pump frequencies vs. test section flow velocity produced by PIV calibration

Hz	(m/s)
2.5	0.060163
5	0.11631
10	0.229375
15	0.347038
20	0.469252
25	0.594034
30	0.727234
35	0.872143
40	1.00542

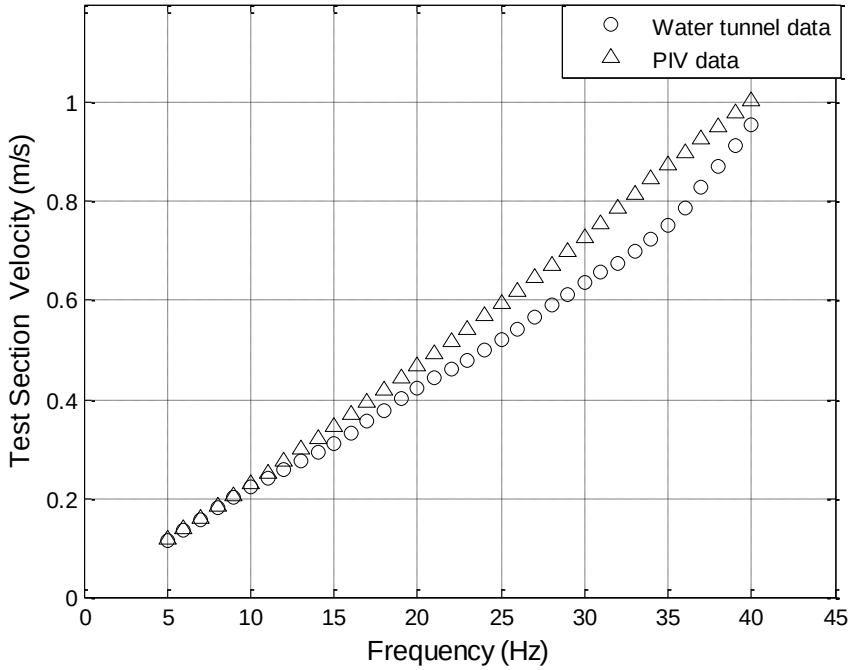

Figure 3.14. Pump frequencies vs. stream velocity for both the water tunnel data and the PIV data

3.3.2. Torque Sensor Calibration. The torque sensor was calibrated, out of the water tunnel, at various times throughout the study. This was done to obtain an accurate relationship between the sensor output signals and the applied torque. A set of similar

weights (8.4477 gm) was used to apply torque forces on a wheel that had a radius of 0.0492125 m (1.937 5 inches). The wheel was attached to the torque sensor assembly horizontal shaft. Both thread and a plastic bag were used to hang the weights tangentially and vertically from the wheel's circumference. The power supply's voltage and current were set to 12 volts and 2 amps, respectively, to ensure no slipping occurred when the weights were added. In order to simulate the torque resulted from different flow speeds acting on the rotor, the weights were added gradually to the bag. The sensor reading in millivolt per volt was averaged and collected for every weight increment by using the data acquisition and LabVIEW code. The data was submitted to an excel sheet where a converting relationship converted the volt signals (mV/V) to torque (N/m) was obtained. Figures 2.15 and 2.16 present the torque sensor calibration setup and the sensor converting relationship, respectively.

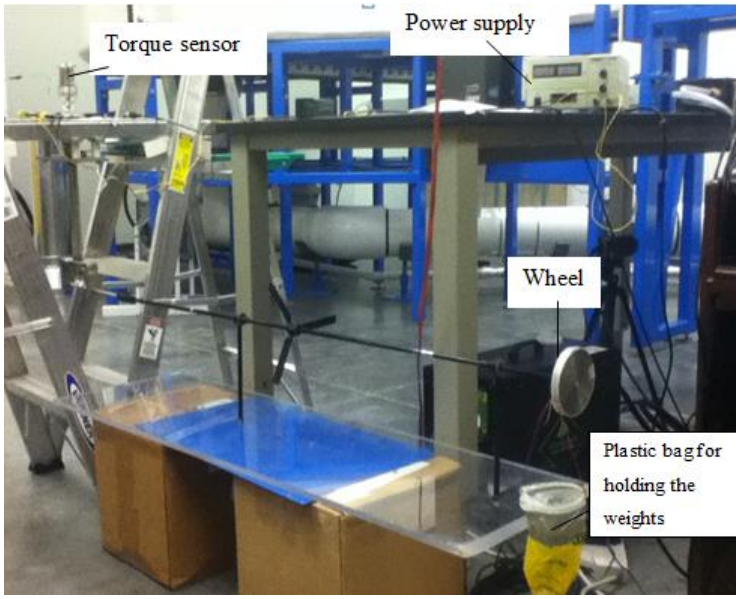

Figure 3.15. Torque sensor calibration setup

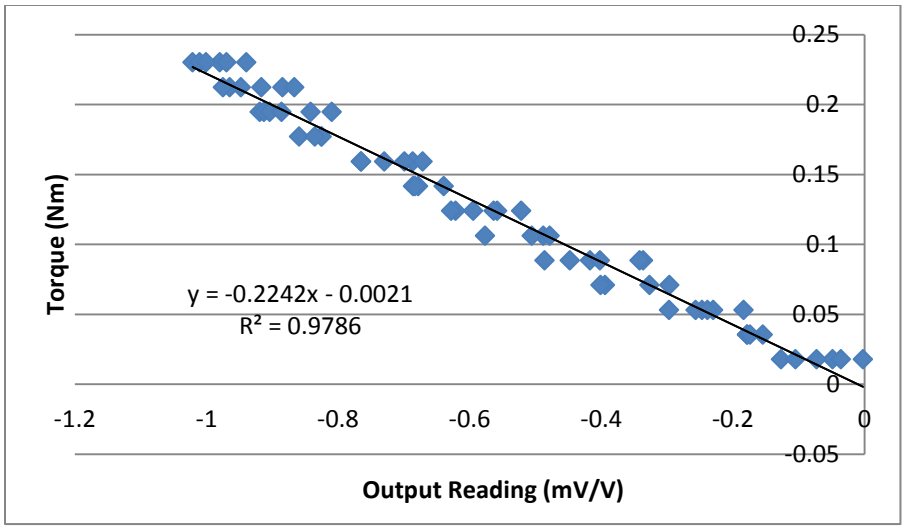

Figure 3.16. Sensor output signals vs. applied torque

3.3.3. RPM Sensor Calibration. An electrical engine (with a speed controller) was used to calibrate the RPM sensor at various rotational speeds. The magnet was attached to the engine's shaft. The Hall Effect sensor was placed at a distance close to the magnet (3 millimeters). Finally, RPM readings were verified at different engine speeds.

The number of pulses was one pulse per revolution because only one magnet was used. As a result of using one magnet, the sensor had a low resolution (resolution is proportional to the number of pulses per cycle). The drawback effect is that, the sensor could not count part of shaft's cycle; it could only count one full cycle each time the sensor passed the magnet. Thus, during detection time, one cycle might be either added to or deducted from the real RPM. Any miscounting was dependent on the magnet's initial position when the shaft began rotating and its final position when the shaft stopped. Because the shaft rotated at a rotational speed between 150 - 660 RPM, the error (which varied between 0.15 - 0.66 %) is acceptable.

3.4. EXPERIMENTAL PROCEDURES AND CONFIGURATIONS

3.4.1. Power Evaluation Experiments. This set of experiments utilized the torque and RPM sensors to measure the generated power by different turbine system configurations.

3.4.1.1 Pitch angle and flow velocity. In the first experiment, the unducted 3-blade single turbine system's performance was examined. This experiment was performed several times at different pitch angles and under different flow conditions. Here, the pitch angles were measured, for the hydrofoil chord, with respect to the plane of rotation, by a digital angle meter. The rotor was, primary, fitted to a vertical shaft to ensure that the rotor was referenced to zero (see Figure 3.17). The angle meter's base was then rested on the blade's lift surface, parallel to the chord. Finally, the blade was adjusted to the desired pitch angle position and the two hub halves were attached firmly.

Figure 3.17. Vertical shaft with rotor referenced to zero

3.4.1.2 Multi-turbine system. A second set of experiments was conducted to investigate the multi-turbine system's (the coaxial-turbine system) performance within different configurations and then compare that performance to both 3- and 6-blade single turbines. All of the configurations were tested at a pitch angle of 20^o. Using this pitch angle allowed better monitoring of the power behavior over a wide range of flow velocities without bending in the rotor blades or failure at the blades' roots under the thrust force at relatively high speeds. The different configurations of the multi-turbine system were arranged to have either two or three rotors attached to the same horizontal

shaft by using setscrews. The axial distance (x) between the rotors was varied to have lengths of either 2D or 4D (where D is the turbine diameter). For each axial distance, the rotors' relative installation angle (the azimuth angle difference ∅) was also changed to either 0^o or 30^o (see Figure 3.18).

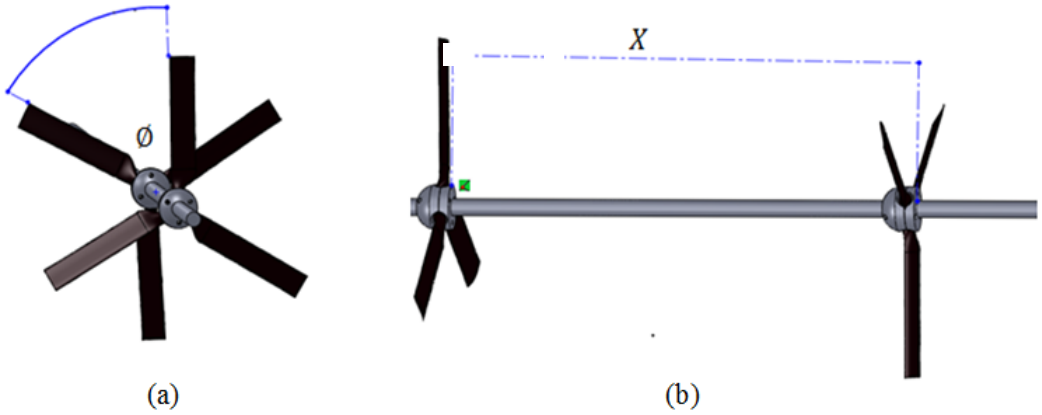

Figure 3.18. Turbine system arrangement (a) the rotors relative installation angle (∅) and (b) the axial distance between rotors (x)

3.4.1.3 Duct reducer. In the third experimental power examination, the duct reducer was utilized to compare performance change in both single and multi-turbine system under enhanced flow speeds. Here, the pitch angle remained the same (20^o) for each system. In the multi-turbine system, the distance between rotors (x) was fixed to 2D due to duct length limitations. The rotors' relative investigation angle (∅) was fixed at 30^o for better turbine performance.

3.4.2. Flow Visualization Experiments. These experiments utilized PIV system to examine the effects of the number of blades, downstream distance, and flow velocity on the wake structure. Study of the wake provides details about the turbine's energy loss at an ambient flow condition. The wake characteristics is an indicator of the stall delay phenomenon due to the rotational effect of the turbine[21]. Moreover, investigation of the far wake region helps in optimizing the turbines arrangement in the farm turbine.

Each run in this experiment used either 3- or 6-blade turbine with a pitch angle of 20^o. The laser sheet was adjusted vertically and aligned with the center of the turbine axis. The experimental procedures and steps used were very similar to those used in the water tunnel calibration experiments. However, in the wake structure investigation experiments, the number of acquired images was increased for every run to 1000 images. As a result, a smoother averaged flow velocity profile was attainable from the turbulent flow regions behind the rotor. Figure 3.19 is an image of the laser sheet, the reference point that centered at the middle of the area of interest, and the rotor located upstream at distance x (x is function of rotor diameter D) from this reference point.

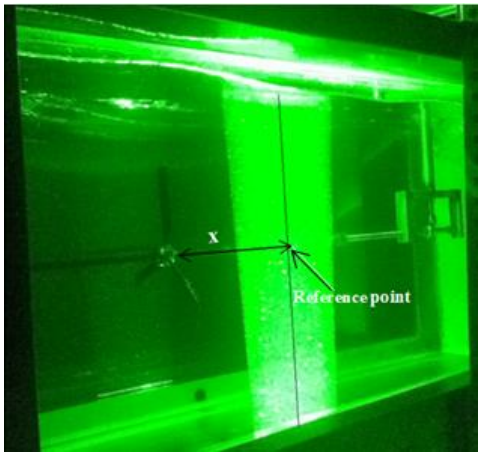

Figure 3.19. Reference point (centered the laser sheet) at distance x behind the rotor

The velocity profile was generated after the processed images were imported to Tecplot 360 software (each run images imported separately). The images were averaged, and the vertical line (the location of the velocity profile) that passed through the reference point was located and extracted from the averaged victor field of the area of interest. (See Figure 3.19 for this vertical line.)

4. RESULTS AND DISCUSSION

Various turbine settings were used during the experimental testes. These settings included the following:

- An unducted 3- or 6- blade single turbine
- An unducted multi-turbine system (containing either two or three 3-blade turbines)
- A ducted 3-blade single turbine
- A ducted multi-turbine system

An untwisted, constant cross-section blade, profile (Eppler 395), was used in all of the experiments. The composite blade's span length was kept the same at 83.82 millimeters (3.3 inches without the root). A description of both the rotors and duct used can be found in Section 3. The water altitude for all experiments was maintained at the same level, 50.8 millimeters (2 inches) from the water tunnel's shoulders edges. This distance was used for two purposes:

(a) Prevent the water from spilling over the walls during running the water tunnel.

(b) Avoid the effect of changing the free surface proximity on the power output [52].

Even though the blockage created by a turbine operating in a channel may increase the potential extracted energy [62, 63], no considerations were taken to correct this increase. The reason was that, all the turbine arrangements had similar small swept area (the blockage created was small, approximately 4.87% of the water tunnel cross-section). Moreover, no numerical simulation models were included in this study (numerical models required experimental validation).

The turbines were exposed to a range of flow speeds so that the flow speed effect on the power (P) and power coefficient (C_p) could be investigated. The flow speed range was varied from the cut in speed (speed at which turbine starts rotating and generating power) to the flow speed of 0.97897 m/s. The applied load was varied by setting the power supplier output volt to 0, 1, 2, 3, 4, and 5 V for each flow velocity in the range. (The current changed correspondingly in the range 0-0.08 A.) This changed voltage

produced a torque magnitude between 0.015 and 0.096 N.m. Proper time was allowed for every voltage change so that the torque sensor reading approach stable state. An appropriate time also was applied between experimental runs so that residual stresses were removed from the torque sensor.

Reynolds number of a scaled model cannot be matched to a full-scale turbine under this flow conditions. Therefore, conventionally, TSR is used. Both C_p and TSR are non-dimensional numbers. Thus, the curve obtained from these two parameters is a good indicator for performance comparison between turbines from similar types but with different sizes [39]. The P versus TSR relationship has a behavior that is similar to the C_P versus TSR relationship. This similarity indicates that either can be used to characterize the turbine system's performance. Therefore, the power against TSR curve, in most of the cases, was not included in this section.

Several set of experiments were conducted at four fixed flow velocities (0.7272, 0.8146, 0.8996, and 0.9789 m/s) to obtain the C_p verses the TSR relationship. The turbine system's loaded torque was increased gradually for each of these flow velocities, at proper increments, until the system came to a complete rest. This gradual increase in the torque caused the TSR to become varied.

Table 4.1 lists (in detail) various cases of turbine system arrangements that were tested in the water tunnel to investigate the power coefficient. The corresponding objectives of each test are listed as well.

Table 4.1. Various conducted power experiments and their objectives

Setting	Variables	Constants	Objectives
Unducted 3-blade turbine	Pitch angle and flow velocity	Applied torque	Investigate the power and power coefficient versus the flow velocity for different pitch angles.
	Pitch angle and TSR	Flow velocity	Investigate the power coefficient versus the TSR for various pitch angles at different fixed flow velocities.
Unducted two 3-blade turbines	TSR	Pitch angle and flow velocity	Investigate the power coefficient change after adding, coaxially, another 3-blade rotor to the turbine system.
Unducted 6-blade turbine	TSR	Pitch angle and flow velocity	Compare the power coefficient of the unducted 6-blade turbine to both the unducted 3-blade turbine and the unducted multi-turbine system cases.
Unducted Three 3-blade turbines	TSR	Pitch angle and flow velocity	Investigate the power coefficient change after adding, coaxially, a third 3-blade rotor to the turbine system.

Table 4.1. Various conducted power experiments and their objectives (cont.)

Setting	Variables	Constants	Objectives
Unducted two 3-blade turbines	TSR and rotors relative installation angle ($\emptyset = 0^{o}, 30^{0}$)	Pitch angle, flow velocity, and distance between rotors (x=2D or 4D)	Investigate the effect of changing the rotors relative installation angle on the two 3-blade turbines system's performance
	TSR and distance between the rotors (x=2D , 4D)	Pitch angle, flow velocity, and rotors relative installation angle ($\emptyset = 0^{o}$ or 30^{0})	Investigate the effect of changing the distance between rotors on the two 3-blade turbines system's performance
Ducted 3-blade turbine	TSR	Pitch angle and flow velocities	Investigate the effect of duct on a 3-blade single turbine's performance. Compare the power curve's behavior with a ducted multi-turbine system's behavior.
Ducted two 3-blade turbines	TSR	Pitch angle and flow velocities	Investigate the effect of duct on performance of a system of two 3-blade turbines. Compare its power curve's behavior with a ducted 3-blade single turbine's behavior.

Table 4.2 lists various PIV experiments that were conducted to investigate wake structure under different changed parameters.

Table 4.2. Various conducted PIV experiments and their objectives

Setting	Variables	Constants	Objectives
Unducted 3-blade turbine	Downstream distance	Flow velocity	Investigate the flow characteristic inside the wake at different axial downstream distances.
Unducted 3-blade turbine	Flow velocity	Axial downstream distance	Investigate the change in flow characteristic inside the wake under different flow velocities.
Unducted 6-blade turbine	Downstream distance	Flow velocity	Investigate the effect of number of blades on both the wake structure and wake rate of recovery.

Due to the large number of conducted experiments and to avoid confusion, calculations and their corresponding plots were achieved through multi-purpose codes. These codes were written in MATLAB scripts. These codes were detailed to provide the user with a variety of ways to monitor the power and power efficiency trend for different selective sets of both single and multi-turbine systems. Only one code is presented in the Appendix B. this script was generated to present the relationship (for selective cases) between the power and power coefficient versus tip speed ratio and the power versus the rotational speed. Only a portion of the overall generated plots are presented in this chapter because they are adequate for the turbine performance investigation.

4.1. UNDUCTED 3-BLADE SINGLE TURBINE

Turbine hydrodynamics is a critical factor in maximizing the turbine's energy output. Optimizing these factors leads to reducing the overall cost of the generated energy. Therefore, it is essential to understand the hydrodynamics governing parameters of HAHkTs.

4.1.1. The Effect of Pitch Angle and Torque on Turbine Performance. Pitch angle (as previously defined in Section 2) is the angle between the blade chord and the plane of rotation. The pitch angle's effects on the turbine's performance was examined through various pitch angles ($\theta = 2^o,\ 5^o,\ 10^o,\ 12^o,\ 15^o, 17^o,$ and 20^o). Multi-purpose codes were used to plot the power and power coefficient (henceforth referred to as P and C_P, respectively) for each pitch angle versus the flow velocity and the TSR. Each data point of the generated power in the plots was initially obtained by multiplying the torque by the rotational speed [see (13)]. A limited amount of experimental data was obtained along the lower region of the TSR. This was due to the turbine cut-out as the angular velocity decreased (load increased). Thus, the power peak was not reached. (This limited data was observed for all the experiments.) This phenomenon could be attributed to the stall delay which is affected by centrifugal forces, hydrofoil shape, and angle of attacks at a local section along the blade's span [64].

The pitch angle's effect on a single 3-blade turbine's performance is illustrated in Figures 4.1 and 4.2. Figure 4.1 was generated to illustrate the P and $C_P$versus the flow velocity for different pitch angles when the applied torque was 0.0153 N.m (Figure 4.1 a, c) and 0.0472 N.m (Figure 4.1 b, d). These results are consistent, demonstrating that both the P and C_P increase as the pitch angle decreases from 20^o to 5^o. Comparing the pitch angles 5^o to 20^o, P and C_P are doubled (at $\theta = 5^o$). This increase occurs because the AoA increases as the pitch angle decreases [see (2)], allowing more lift to be exerted by the flow on the pressure side of the blade [37]. Another observation is that, the P increases at a specific pitch angle as the flow increases. These increases occur because higher kinetic energy flux passes the rotor's swept area [see (15)]. In the other hand, this increase in axial velocity (U) (under fixed applied torque) causes the turbine's angular velocity (ω) increases faster (the ratio U/ω decreases). As a result, AoA decreases,

which in turn decreases the C_P exponentially. A hydrofoil section located at 80% of the blade span was examined to validate this decrease in AoA. (This 80% is a reasonable span for the design investigation [37]). Here, the blade's pitch angle was set to 5^o, and the applied voltage was 0V (0V means the torque is approximately 0.015 N.m). The AoA decreased from 8.2271^o to 4.3418^o as the flow velocity increased from 0.4939 to 1.0054 m/s. Thus, at a higher free stream velocity, a higher relative velocity (U_r) strikes the pressure side of the blade with a smaller AoA, Thus, a smaller percentage of the available kinetic energy was captured. Consequently, a relatively higher P and a lower C_P may be resulted (as compared to the lower flow velocity).

Equation 15 shows the power generated by a turbine as a function of flow kinetic energy and turbine efficiency.

$$P = \frac{1}{2}\rho U^3 C_p A \tag{15}$$

where ρ is the water density, U is the flow velocity, C_p is the turbine system's efficiency, and A is the swept area.

Figure 4.1 also illustrates that both P and C_P increased as the applied torque increased. For example, the maximum power produced by a turbine with a pitch angle of 5^o, under an applied torque of 0.0153 N.m, was 0.9294 W (Figure 4.1 a). The power output under the same pitch angle and inflow condition was 3.0486 W when the applied torque was 0.0472 N.m (Figure 4.1 b). An increase in torque forces the turbine to reduce its rotational speed, increasing the AoA. This increase in AoA results in higher lift subsequently larger torque.

Another observation was that, decreasing the pitch angle (at specific flow conditions) was always combined with increase in the rotor's angular velocity. However, the turbine tends to cut out at lower flow velocity due to a lower generated torque.

Reducing the pitch angle beyond 5^o (e.g., to 2^o) produces a lower P and a lower C_P. This reduction could be related to the small pitch angle (and thus a large AoA) causing the turbine blades to operate at a stalled AoA. Also, blades pitched to angles less

than 5^o bent (under the effect of thrust force) more than the blades pitched to angles higher than 5^o. This bending could ultimately affect the rotor's performance.

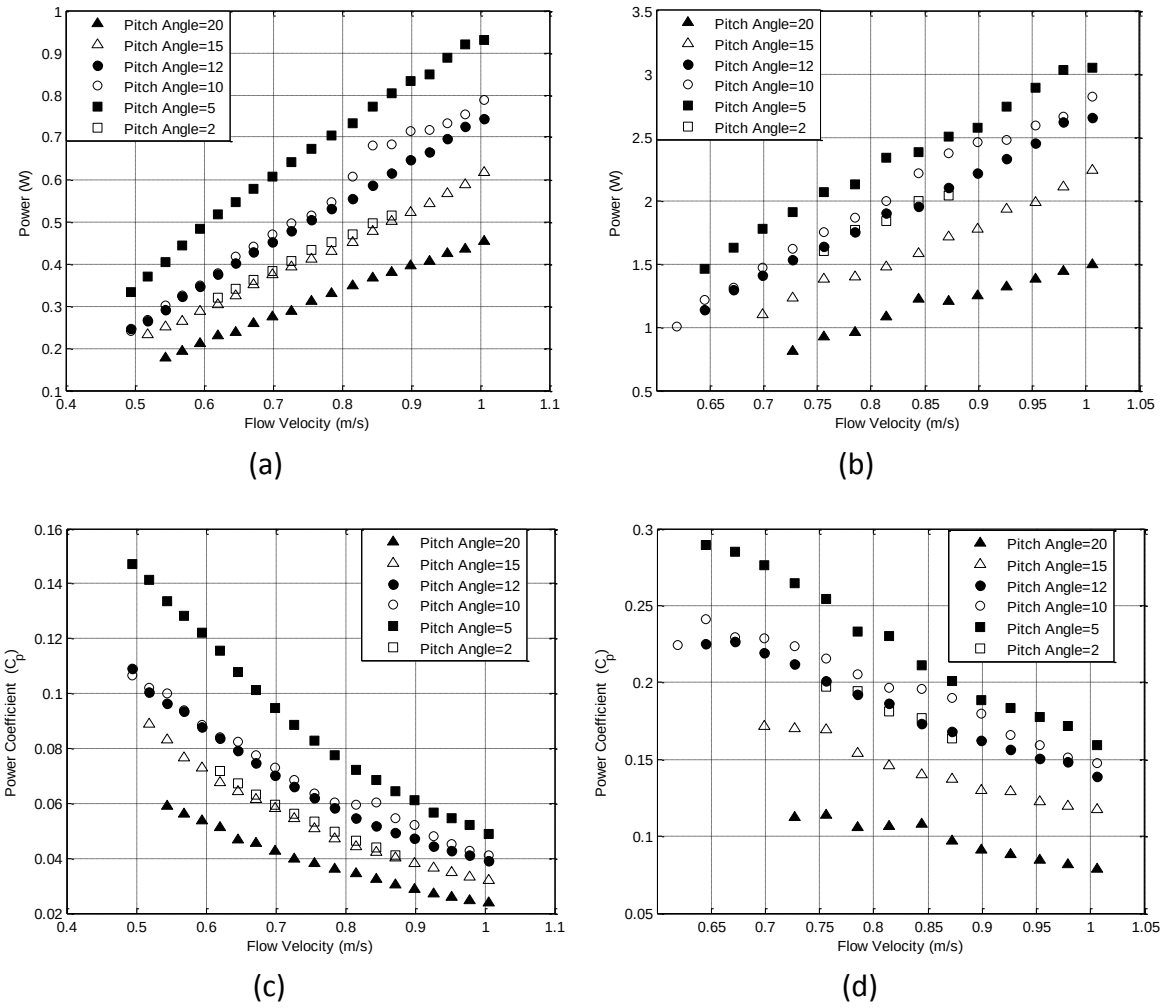

Figure 4.1. Power and power coefficient vs. flow velocity for different pitch angles. The applied volt is (a,c) volt =0V and (b,d) volt = 3V.

Figure 4.2 was generated to illustrate the effects of TSR on C_P at various pitch angles. The results in this figure follow the same trend as thus plotted in Figure 4.1 (the pitch angle of 5^ohad the highest C_P). The C_P peak (in Figure 4.2) has leftward shift and lower magnitude as the pitch angle increases. Decreasing the pitch angle would likely increase the range of the optimum TSR which was also observed in [54]. In general, C_P increases for all pitch angles as the TSR decreases. This was due to increasing the AoA along the blade length (see Figure 4.3). The relationship (in Figure 4.2) is linear at the

right side of the curves (e.g., at a TSR greater than 5.75 when the turbine has pitch angle of 5^o). A large percentage of the blade's length (approximately 65% of the untwisted part of blade; see Figure 4.3) operates either below or close to the stall AoA. Reducing the TSR so that it is near its optimum value will reduce the rate of increment of C_P. (The optimum value was not achieved in this study because the turbine cut out.) The C_P slop declined because a larger portion of the blade's length operated above the stall AoA. This trend is illustrated in Figure 4.2 when ($4.8 < TSR < 5.5$, for pitch angle of 5^o). At even lower TSR regions (beyond the peak) the C_P will decrease. This drop in power is ascribed to that, the decline of TSR results in increasing the AoA along the blade span. At this limits of AoA, most of the swept area of the turbine blades operates under the effect of the stall. (Most of the blade is above the stall AoA) [64].

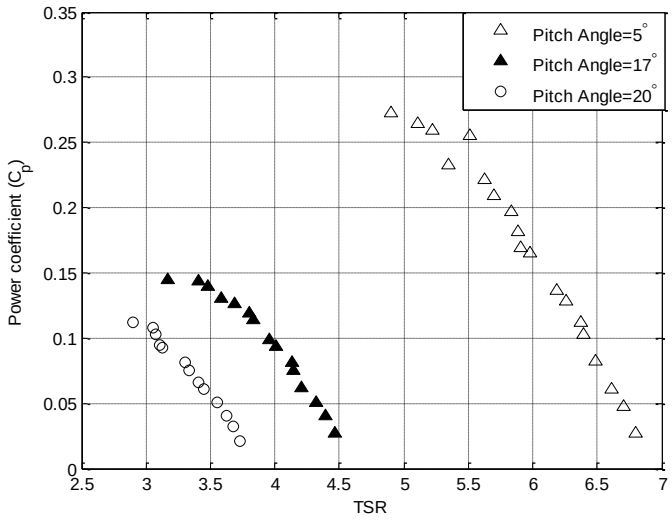

Figure 4.2. Power coefficient vs. TSR for 3-blade unducted turbine. Different pitch angles of 5^o, 17^o, and 20^o were tested at flow speed of $U_\infty = 0.9789$ m/s.

Figure 4.3 was generated based on several known hydrodynamic parameters (TSR, free stream velocity (U), and pitch angle (θ)). A 2D model of the Eppler 395 hydrofoil was used to calculate the stall AoA numerically. Quad-4 elements were used to mesh this model in ANSYS ICEM CFD. A CFD analysis conducted in ANSYS 12.0 was

then used to solve the problem. The steps followed can be found in [35]. This stall AoA could be higher because the 2D problem did not consider the effect of either centrifugal or Coriolis forces produced by the blade's rotation.

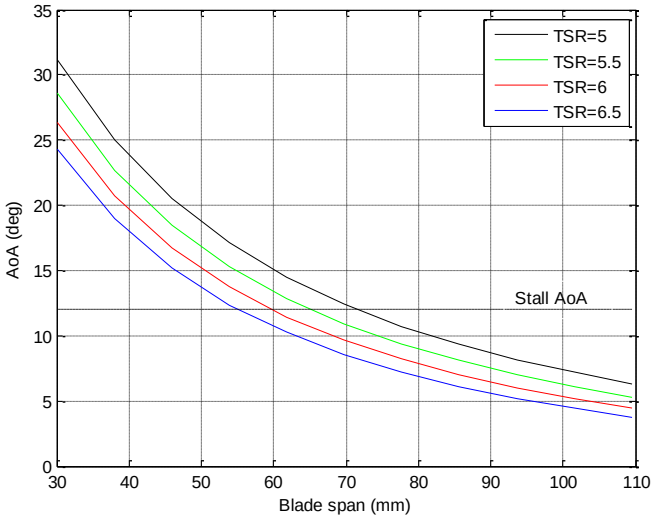

Figure 4.3. An AoA along the blade's span when the pitch angle is 5^o and the flow velocity is $0.9789\ \mathrm{m/s}$.

4.1.2. The Effect of Flow Operating Conditions on Turbine Performance.

Different four free stream velocities and fixed pitch angle ($\theta = 20^o$)were used to investigate the effect of flow velocity on P amd C_P vs. TSR. This fixed pitch angle was used for all of the remaining experiments. At specific TSR, both P and C_p are proportional to the flow stream velocity as more kinetic energy becomes available (see Figure 4.4 a and b). However, the $C_p$in the Figure 4.1 has a non-proportional relationship with the flow velocity. The C_p here is higher at higher flow velocities because at a specific TSR, the turbine's rotational speed will be greater when it is exposed to a higher flow. The applied torque must be higher for this turbine to operate at the same TSR as when it is exposed to a lower flow. Based on the flow conditions and hydrofoil shape, this higher torque may result in large increase in the AoA. Because this AoA is much larger than when the turbine is exposed to a lower flow velocity, the yielded C_p is higher.

To confirm this finding does not conflict with the data illustrated in Figure 4.1, arrows were drawn to aim at arbitrary group of four points that were generated when the turbine was loaded with a specific torque and exposed to different four flow velocities (see Figure 4.3 b). This figure is consistent with the data plotted in Figure 4.1; the C_p decreases as the flow velocity increases if the torque is fixed.

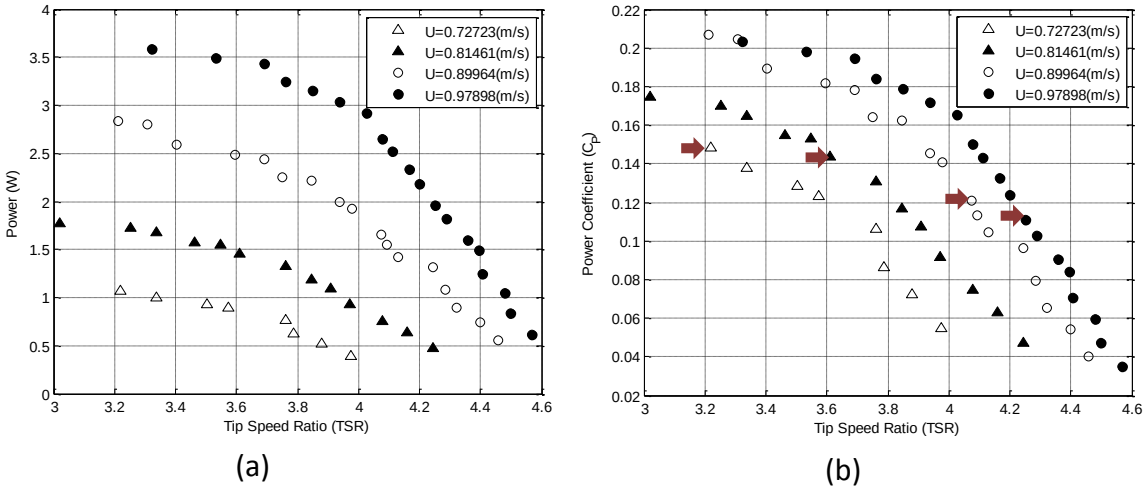

Figure 4.4. (a) Power and (b) power coefficient vs. TSR for unducted 3-blade single turbine exposed to different flow velocities.

4.2. UNDUCTED 6-BLADE TURBINE AND MULTI-TURBINE SYSTEMS

The hydrodynamic performance of an HAHkT is affected by the solidity, the number of blades, and the TSR. These parameters control the fluid flux through the turbine rotor, which can be employed to maximize the power extraction [21]. The optimum turbine solidity and blade numbers occurs when the turbine produces a maximum C_p at a given TSR. Any change in either of these two parameters (from their optimum state) decreases the C_p. In the one hand, a turbine without blades provides zero lift. In the other hand, a turbine with an infinite solidity blocks the flow and provides zero mechanical work. Thus, the optimum values of solidity and number of blades exist, at a given TSR, between these two extremes. The number of blades that can be added to a

rotor is limited by either geometry or a high solidity. The number of blades in this study was increased by adding, coaxially, more 3-blade rotors to the turbine system shaft. (The 3-blade HAHkT with untwisted blades was approved to generate more power than turbines with either 2- or 4-blades that had the same solidity [21].) For a given solidity, a turbine with 4 blades or more is associated with higher blockage (at a specific TSR). Thus, less energy flux passes the rotor, resulting in less power extraction [21]. Adding more rotors to the turbine system reduces the blockage resulted from adding more blades to the same rotor (reduces the solidity). This technique may enhance the turbine system performance (increases C_p) under a given flow condition. Additionally, the multi-turbine system needs only one generator to operate, reducing the installation cost of the cables and generators. Grid connection also reduced which decreases the electricity losses to the ambient [8].

4.2.1. The Effect of Increasing the Number of Blades and Rotors. Figures 4.5 and 4.6illustrate that increasing the number of blades (by either adding blades to a rotor or adding second rotor) increases the power extraction at lower flow velocities. Comparable power is generated at high flow velocities. Rector et al. [54] observed a similar behavior in a 6-blade horizontal axis wind turbine (HAWT). For example, at water speeds that were lower than 0.57 m/s (for the multi-turbine system, Figures 4.5 a) and lower than 0.78 m/s (for the 6-blade turbine, Figures 4.6 a) these turbines extracted more power than the 3-blade single turbine. The AoA is very large when a turbine begins to rotate. Thus, the rotor is driven, primarily, by the drag forces exerted by incoming flow on the blades. Systems with a higher number of blades have more drag and a higher torque than that of the 3-blade turbines; systems with an increased number of blades have more surfaces exposed to the flow. Consequently, they can cut in earlier and extract more energy at a lower speed region [54]. The three 3-blade turbine system exhibited the same behavior (extracted higher power at low speed than the two 3-blade turbine system and the 6- blade sing turbine).

Increasing the load from 0V (0.015 N.m) to 4V (0.0677 N.m) caused the curves point intersection to shift right (e.g., the intersection point shifted from 0.57 to 0.78 m/s in Figure 4.5). Moreover, the difference in the cut-in speed between both the 6-blade

turbine and multi-turbine system with 3-blade turbine increased as the applied torque increased. Improving the turbine's performance at lower flow velocities will increase the number of rivers that can be used as a viable site for power generation [54].

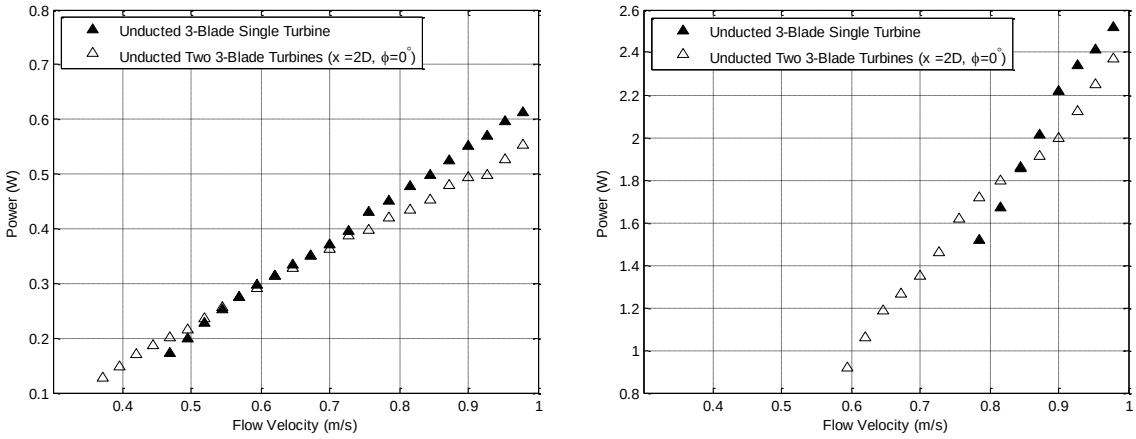

(a) (b)

Figure 4.5. Power vs. flow speed for both an unducted 3-blade single turbine and a system of unducted two 3-blade turbines. The applied volt was (a) 0V, and (b) 4V.

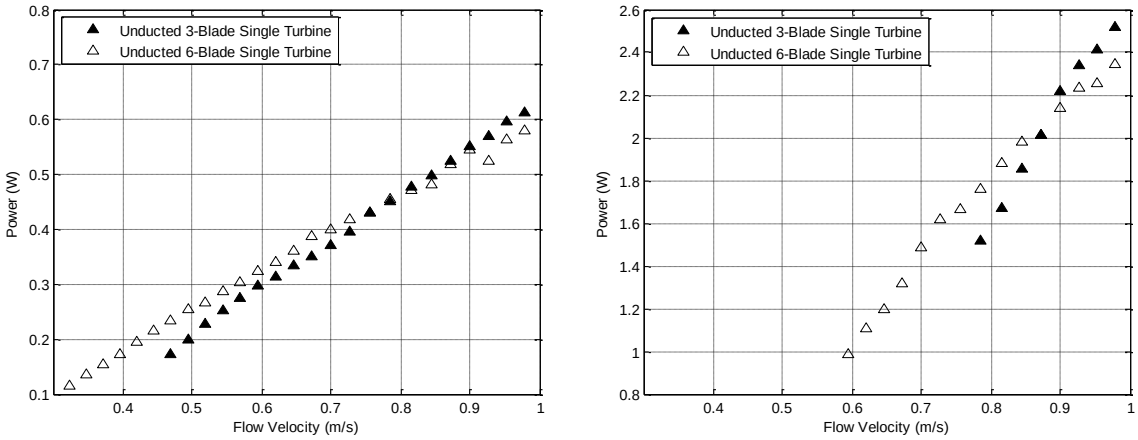

(a) (b)

Figure 4.6. Power vs. flow speed for both an unducted 3-blade single turbine and an unducted 6-blade single turbine. The applied volt was (a) 0V, and (b) 4V.

The following two differences exist between the C_p curves for the different turbine configurations illustrated in Figure 4.7.

1) The maximum C_p reached by systems with more blades increased more than did the 3-blade single turbine.

2) The operational TSR at maximum performance decreased in the higher blade number turbine systems.

The improvement in C_p was expected due to the higher blade surfaces are exposed to the flow compared to the 3-blade single turbine which resulted in higher lift force. The left shift in the operational TSR could be attributed to the decline in the stream velocity through the rotors of both multi-turbine and 6-blade turbine systems. The multi-turbine system has a rotor (the downstream rotor) that is exposed to a lower flow velocity due to the wake effect. The 6-blade turbine is affected by the higher blade number. This higher blade number causes higher flow impedance that lowers the stream velocity through its rotor.

Decreasing TSR and increasing the flow velocity increases the AoA [see (2), (3), and (7)]. An increased AoA produces more lift and torque, but only if the AoA remains below the stall. Adding either another rotor or more blades to a rotor increased the extracted power (at a low TSR region) relative to the 3-blade turbine (see Figure 4.7). For example, when the flow was 0.9789 m/s and the TSR was 3.3 (Figure 1.7 a), the two 3-blade turbine had an increased efficiency of 50% (as compared to the 3-blade single turbine). This increase occurred because the turbine with a lower blade number may operate under significant stall at a lower TSR. The remaining two configurations (with a higher blade number or rotors) may not due to the reduced streamwise flow velocity that reduces AoA below the stall AoA [21, 53].

When a third rotor was added to the multi-turbine system and compared to the two 3-blade turbine system and 6-blade single turbine, the results showed the same behavior in the previous comparison. The system that contained three rotors had a higher C_p that shifted to the lift (lower TSR region); see Figure 4.8. Nevertheless, the resulted improvement in the performance was less for this configuration than it was for the two 3-blade turbine system. The multi-turbine system rotors acted collectively to increase the

extracted power. But due to that the third rotor operated under lower flow velocity than the second rotor; its contribution to power generation was less.

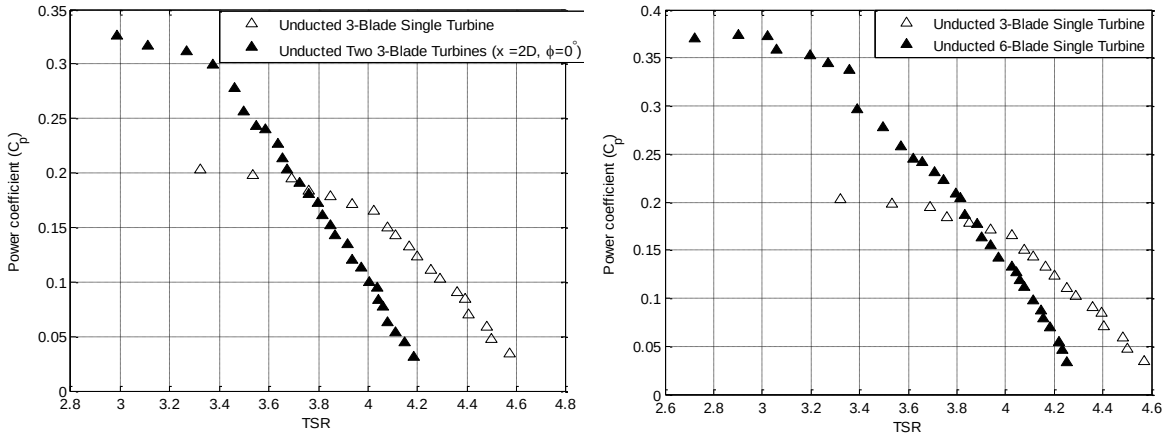

(a) (b)

Figure 4.7. Power coefficient vs. TSR for an unducted 3-blade single turbine as compared to (a) a system of unducted two 3-blade turbines and (b) an unducted 6-blade single turbine at flow velocity of $U_\infty = 0.9789\text{m/s}$

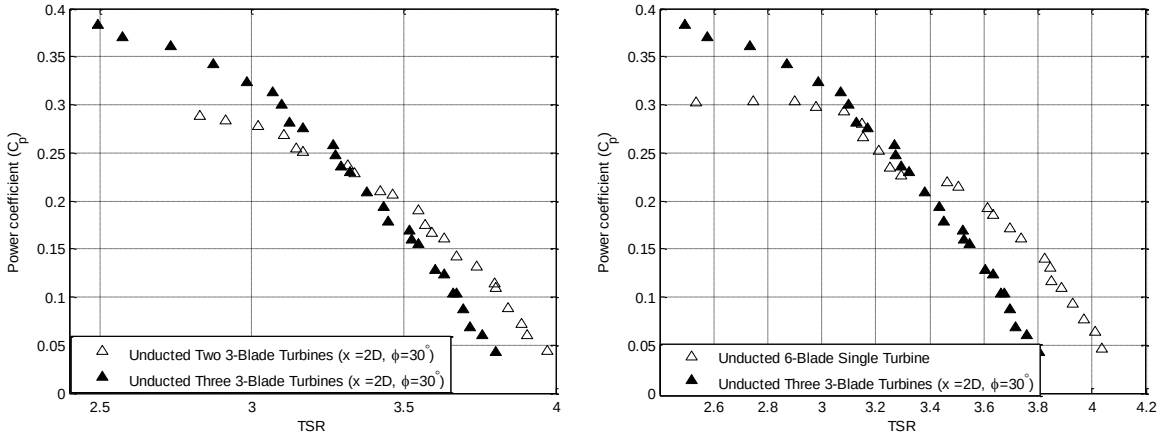

(a) (b)

Figure 4.8. Power coefficient vs. TSR for a system of unducted three 3-blade turbines compared to (a) a system of unducted two 3-blade turbines and (b) an unducted 6-blade single turbine at flow velocity of $U_\infty = 0.8146$ m/s.

The difference in performance between an unducted two 3-blade turbine system and a 6-blade single turbine was examined. These two systems had the same number of blades but operated under different conditions. The multi-turbine system had three blades (the second rotor's blades) operated under lower flow velocity due to the wake effects. The 6-blade single turbine had a higher solidity that reduced the streamwise velocity through its rotor due to higher impedance. At a flow velocity of 0.7272 m/s (Figure 4.9 a), the 6-blade turbine generated more power than the two 3-blade turbine system; the entire curve generated by the multi-turbine system shifted slightly to the bottom. (The $C_p$decreased by approximately 0.042.). This could be attributed to the velocity deficit effects on the second rotor. Moreover, the 6-blade turbine has a hub that is slightly larger than that of 3-blade turbine. Nevertheless, the two C_p curves have a similar shape. They also tend to approach each other as the flow velocity increases to 0.9789 m/s (see Figure 4.9 b). This behavioral pattern was detected in all multi-turbine system arrangements.

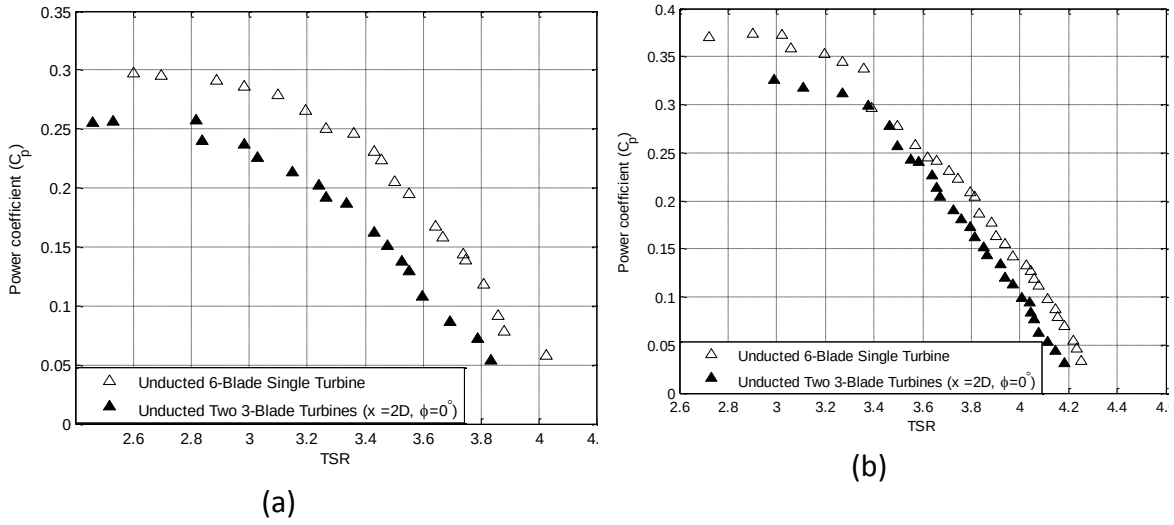

Figure 4.9. Power coefficient vs. TSR for a system of unducted two 3-blade turbines compared to an unducted 6-blade single turbine at different flow velocities (a) $U_\infty = 0.7272$ m/s and (b) $U_\infty = 0.9789$ m/s.

4.2.2. The Effect of Relative Installation Angle and Axial Distance. Four experiments were conducted to determine the power output's response to a change in two experimental variables: ∅, and x. (These variables are defined in Section 2.1.2.) The effect of the rotors relative installation angle (∅), when the flow speed was $0.9789\ \mathrm{m/s}$ is presented in Figure 4.10. No obvious change occurred in the generated power curves when ∅ was varied, neither when x=2D nor x=4D. When x=4. All the power curves generated under lower flow velocities ($0.7272,\ 0.8146$, and $0.8996\ \mathrm{m/s}$)exhibited the same behavior as in Figure 4.10 b. (These result figures are not shown in this thesis). However, the multi-turbine system, at these lower flow velocities with an axial distance between its rotors set to x=2D, generated power that varied with (∅). The output power curves generated when $\emptyset = 30^o$ were slightly higher than that generated when $\emptyset = 0^o$. This increase could be related to the proximity between the rotors (x=2D). This small axial distance made the second rotor's blades performance (under low flow velocity) affected by the blades position in the frontal rotor.

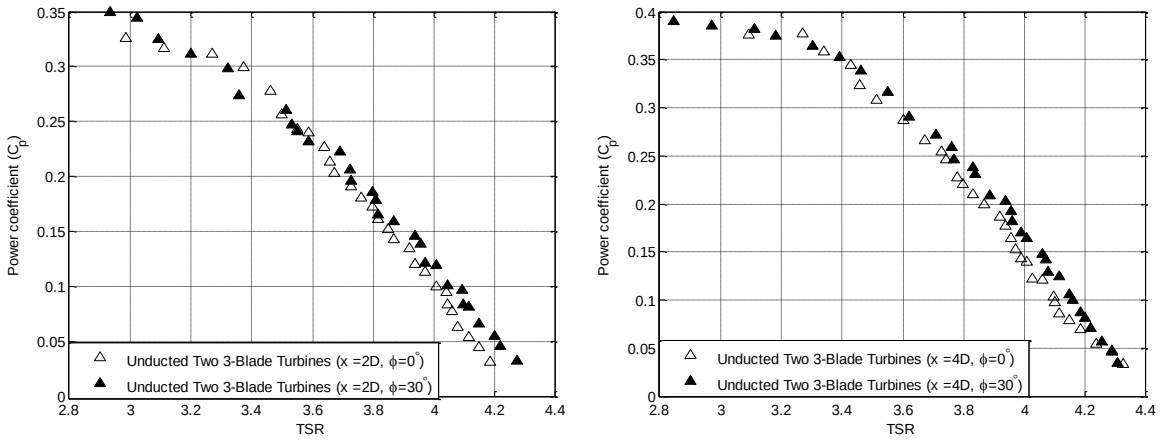

Figure 4.10. Power coefficient vs. TSR for a system of unducted two 3-blade turbines with a fixed distance between the rotors (a) x= 2D and (b)x= 4D. The rotors relative installation angle was varied ($\emptyset = 0^o, 30^o$) and the flow velocity was set to $U_\infty = 0.9789\ \mathrm{m/s}$.

Figure 4.11 compares C_p curves to TSR curves generated by a system of two 3-blade turbines with different axial distances (x=2D, 4D) between its rotors. The rotors relative installation angle for these distances (x=2D, 4D) was fixed either to $\emptyset = 0^o$ or $\emptyset = 30^o$. These configurations were used to examine the effect of changing the axial distance between the rotors on the power generation. The results gathered suggest that the power output improved as the axial distance increased. An improvement in C_p for the system with axial distance of 4D was observed to be 10% and 20 % at TSR of 2.3 and 3.7, respectively, compared to the other system configuration (x=2D); see Figure 4.11 b. This occurs because the axial velocity deficit created by the first rotor decreases as the downstream distance increases (the axial velocity increases with x).

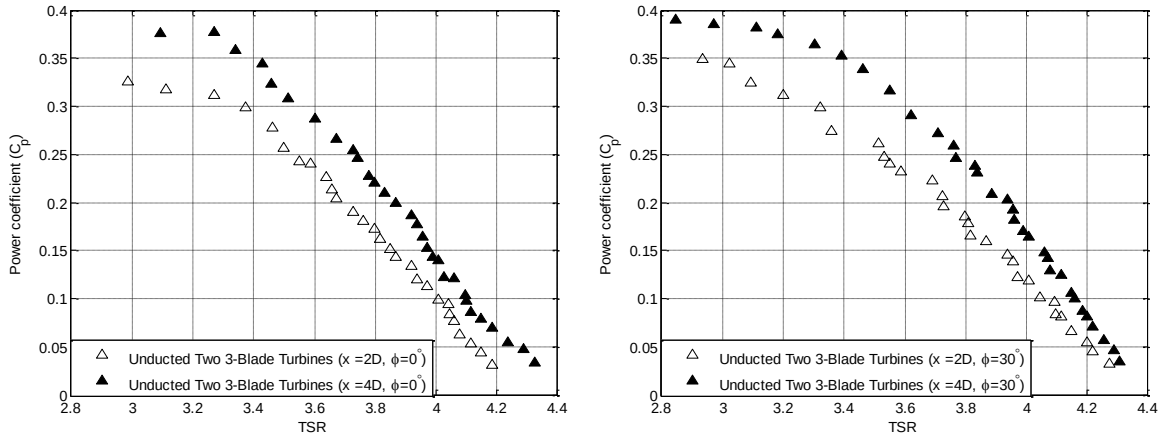

(a) (b)

Figure 4.11. Power coefficient vs. TSR for a system of unducted two 3-blade turbines with a fixed rotors relative installation angle (a) $\emptyset = 0^o$and (b) $\emptyset = 30^o$. The distances between the rotors was varied (x= 2D, 4D) and the flow velocity was set to $U_\infty = 0.9789$ m/s.

4.3. TURBINE SYSTEMS WITH DUCT REDUCER

A duct placed around a rotor significantly enhances the rotor's flow rate as water passes through its swept area. Therefore, the extracted power by a ducted turbine is also higher than that extracted by a bare turbine [56, 59]. Two design factors can be added to

the existing duct reducer to improve its performance: an end diffuser and a flange. Attaching a diffuser at the end of the duct reducer (attached to the pipe exit) gradually adjusts the flow that passed through the rotor to the ambient conditions [56]. An additional flange around the diffuser's exit circumference increases the formation of vortices at the downstream region. More water is drawn to flow through the diffuser because these vortices surrounded by low pressure regions [59]. Unfortunately, these two design factors were not applied because the water tunnel's size was limited.

These experiments were conducted not only to monitor the change in generated power for ducted and unducted 3-blade single turbine and multi-turbine system individually, but also to compare their responses after using the duct. The power coefficient of both ducted and unducted 3-blade single turbines as a function of TSR is illustrated in Figure 4.12 a. These results confirm the inherent advantage of using a duct: the ducted turbine's output power is increased due to the increased flow velocity that passes through its rotor. Improvement at the maximum reached C_p, before the ducted 3-blade single turbine cut out, was between 260 and 310% for different inflow velocities (between 0.7272 to 0.9789 $\mathrm{m/s}$ respectively). The same relationships for both the ducted and the unducted system of two 3-blade turbines are plotted in Figure 4.12 b. Similar to the single turbine, the multi-turbine system's performance was enhanced by a duct. The curves that describe the C_p against TSR for the ducted multi-turbine system was not completed until the turbine cut out because the clutch reached its maximum design torque (0.226 N.m). Loading the clutch with a higher voltage (to increase the turbine applied torque) resulted in significant fluctuation in the torque sensor reading. Thus, power collected data was inaccurate.

The ducted system's power curves were also observed to shift dramatically to the right. It can be inferred that the C_p peak of the ducted turbines occurred at a higher TSR. The velocity is high around the rotor with the duct. Thus, high TSR requires the turbine to rotate at a very fast angular velocity. This high rotational speed may eliminate the low speed gear box, which is one of the most expensive parts in the turbine system [55].

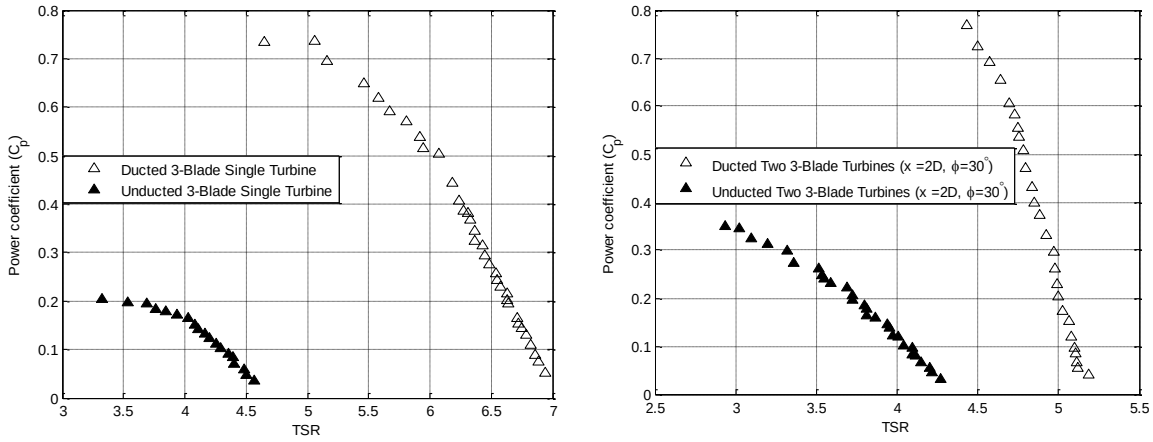

Figure 4.12. Power coefficient vs. TSR for an unducted and a ducted (a) 3-blade single turbine and (b) system of two 3-blade turbines under a flow velocity of $U_\infty = 0.9789\ \mathrm{m/s}$.

Figure 4.13 illustrates a comparison between ducted 3-blade single turbine system and ducted two 3-blade turbine system at different flow velocities. The intersection between the curves is similar to that plotted for the unducted cases (Figure 4.7). The intersection point tends to occur at a higher C_p and a lower TSR as the flow increases. For example, at a flow speed of $0.7272\ \mathrm{m/s}$, the C_p and TSR are 0.558 and 5.16, respectively. At an increased flow speed of $0.9789\ \mathrm{m/s}$, these variables become 0.7234 for C_p and 4.5 for TSR. The curve for the two 3-blade turbine system was not completed at a high flow of $0.9789\ \mathrm{m/s}$ (Figure 4.13 b) because, again, the clutch's capabilities were limited.

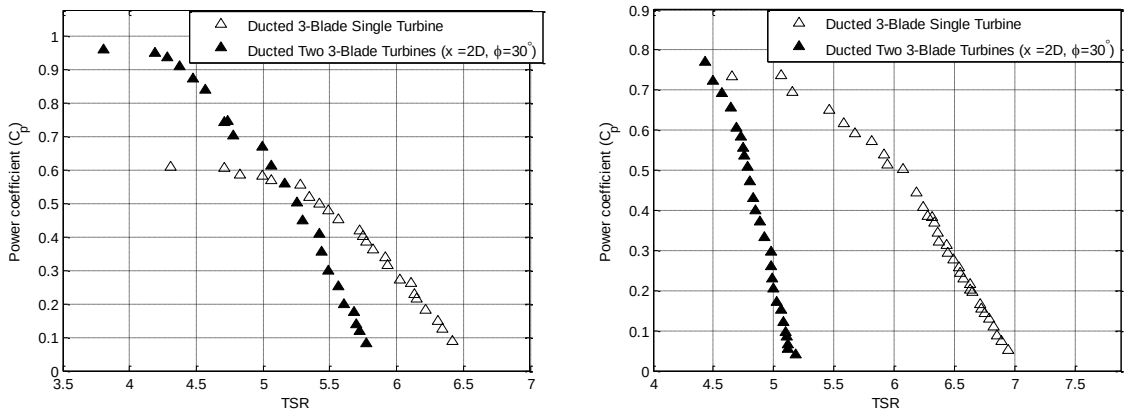

Figure 4.13. Power coefficient vs. TSR for both a ducted 3-blade single turbine and a system of ducted two 3-blade turbines. Flow velocities were set to (a) $U_\infty = 0.7272$ m/s and (b) $U_\infty = 0.9789$ m/s.

4.4. WAKE INVESTIGATION

In the experiments concern the effect of axial downstream distance and number of blades (or solidity) on the wake behavior; the flow speed was fixed at 0.594034 m/s. The rotor was referenced to a reference point downstream so that the axial distance effect behind the rotor could be investigated. This reference point was centered at the middle of the area of interest. Then the camera was used to capture particle images from the illuminated area of interest (see Figure 3.19). The rotor was moved, for each run, (with respect to this reference point) to different axial locations (1D, 2D, 3D, 4D and 5D, where D represents the rotor's diameter). The final step of wake study involved examining the flow speed effect on the wake characteristics. Here, the flow speed was varied to 0.347038, 0.469252, 0.594034, and 0.727234 m/s. The rotor was mounted at a fixed location of 4D from the reference point.

The velocity data presented in each of the wake study figures was collected at a vertical centerline passed the reference point. These data, then, normalized by the free-stream velocity(U_∞). The vertical radial distance from the hub center was normalized by the tip radius R. Finally, the relations were ploted.

Figures 4.14 a and b illustrate a wake decay and expansion. Overall, the wake's width increased slightly and the axial velocity deficit decreased as the flow traveled downstream. Thus, the axial velocity profile tended to recover to the undisturbed velocity as it streamed further behind the turbine. The upper half of the velocity profile (at 1D) has varying slope, indicating the axial velocity distribution fluctuated. This fluctuation could have been caused by the interference that occurred between the free surface and the turbine tower.

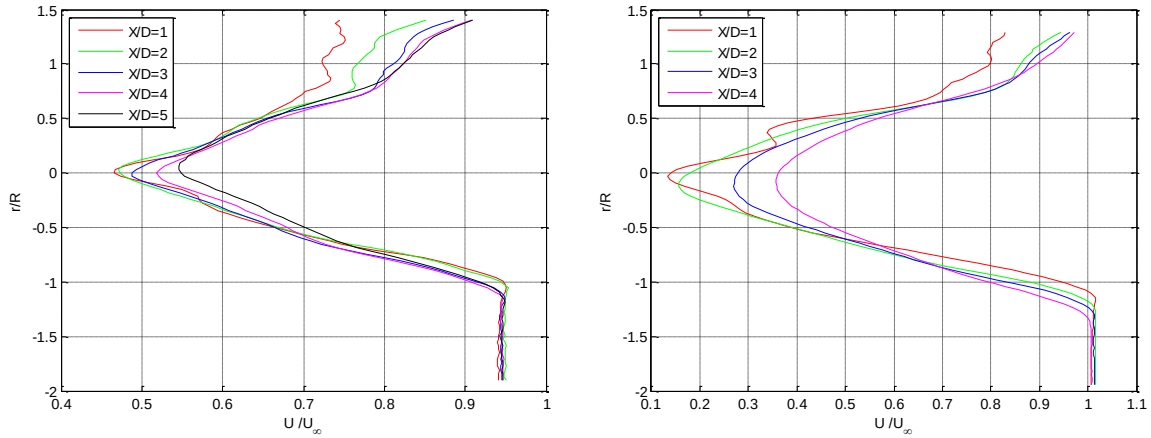

Figure 4.14. Axial velocity profile at different downstream locations for (a) a 3-blade turbine and (b) a 6-blade turbine

The axial velocity profiles behind the 3- and 6-blade turbines are plotted together for comparison in Figure 4.15. This comparison reveals that the velocity deficit behind the 6-blade turbine is higher than it is behind the 3-blade turbine. This indicates that more kinetic energy was observed by the 6-blade turbine rather than escaped its rotor. Also, increasing the number of blades (and therefore, the solidity) resulted in higher flow impedance. The same result was observed when 3D simulation was used [21]. The highest axial velocity deficit was always located at the wake's center. Therefore, the axial wake centerline velocity deficit trend was investigated for both 3- and 6-blade turbines along a path length of 4D. The data collected in this study was limited; however, a

Clamped Cubic Spline Polynomial was used for interpolation and to fit the curves. The rate of recovery for the axial velocity, through regions within two rotor diameter (2D) behind the rotor, was small (see Figure 4.16). However, regions beyond 2D exhibited a relatively higher rate of recovery in the axial velocity profile. This dissipation in velocity deficit was driven by the turbulent intensity in ambient flow. Overall, the velocity deficit produced by a 6-blade turbine had a faster rate of recovery than did the 3-blade turbine. The 6-blade curve also exhibited a gradual decrease in the slope toward 4D. Thus, further downstream locations should be investigated.

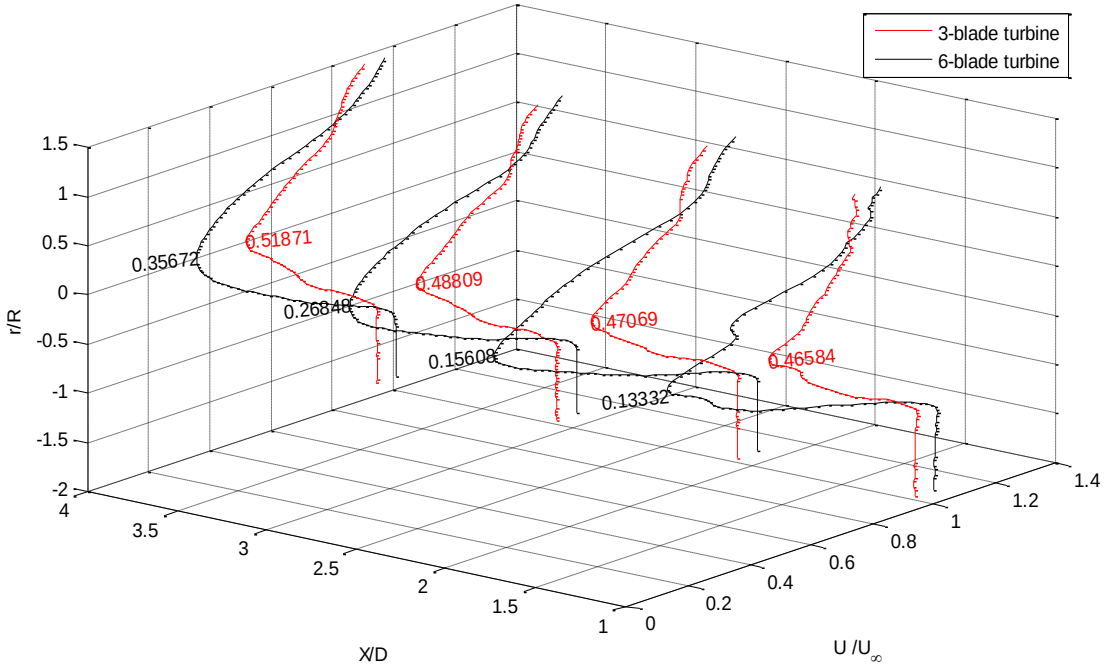

Figure 4.15. Axial velocity profile for both 3- and 6-blade turbines at different axial locations

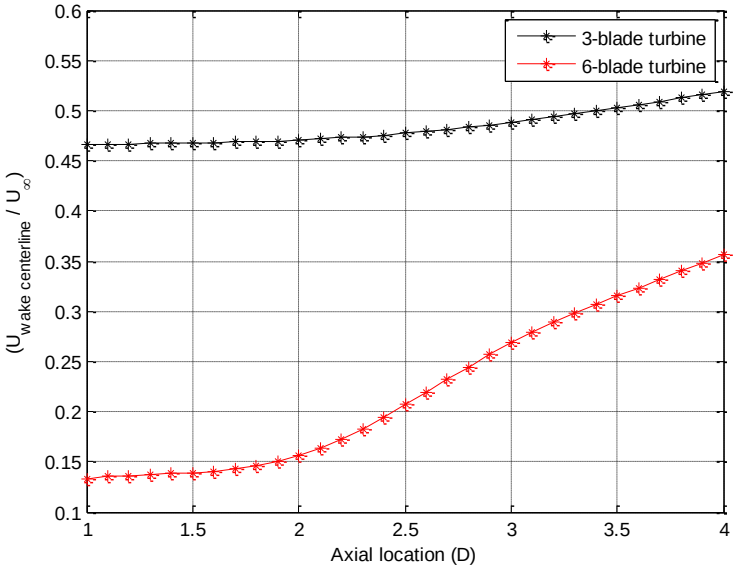

Figure 4.16. Centerline axial velocity deficit at different axial locations for both 3- and 6-blade turbines

The normalized normal velocity component in the wake regions was found to be relatively smaller than the normalized axial velocity component (see Figure 4.17). This observation indicates that the axial velocity is the dominate velocity component when determining the extracted power. The maximum normal velocity is near the rotor's lower tip and hub center. The near tip high normal velocity could be due, in part, to the rotor's blockage, creating a faster flow between the rotor and the water tunnel bed. The flow in the lower part of the wake tends to move downward (negative y direction) while the flow in the upper part moves upward. This was as a result of the radial flow effect. This flow behavior was because the velocity profile was obtained at a vertical line normal to the hub axis. If the normal velocity data had been extracted from either side of the rotor center, the profile shape could have been different because the radial flow is always streams outward the center. Therefore, a better investigation of the radial and tangential flow velocity components can only be achieved if a cross-stream laser plane is utilized.

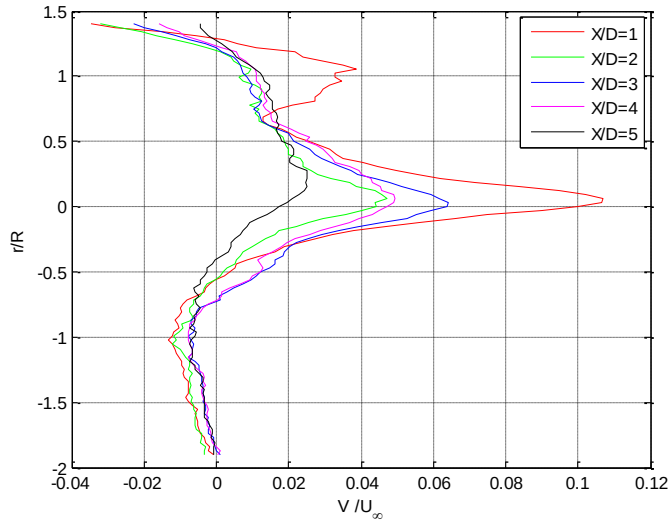

Figure 4.17. Normal velocity profile at different downstream locations for a 3-blade turbine

Varying the flow stream velocity affects the wake velocity. Increasing the flow velocity shifted the axial velocity profile to higher values (to the right). The axial velocity deficit (U/U_∞), however, had a similar profile trend, as illustrated in Figure 4.18. The curves in this figure were generated at a distance of 4D from the rotor. The flow velocity was varied. The data in this figure suggests that the flow deficit (the wake characteristics) is poorly affected by the incoming free stream velocity.

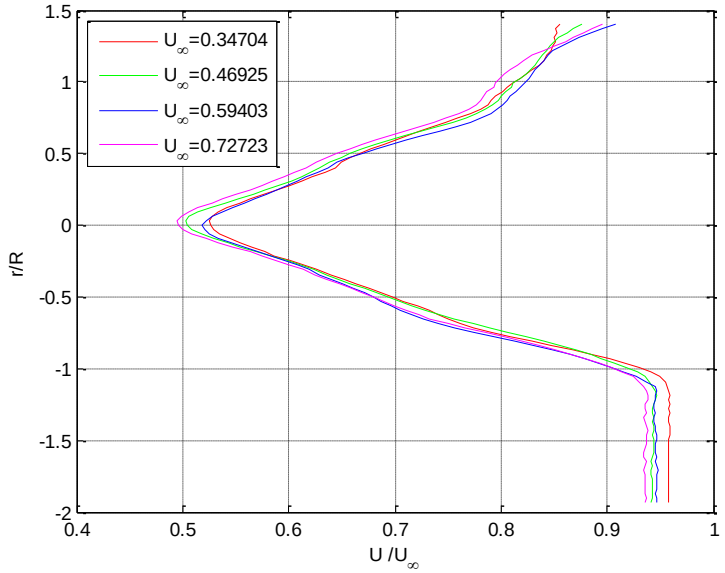

Figure 4.18. Axial velocity profile for different flow velocities at a fixed axial location (4D)

5. CONCLUSION AND FUTURE WORK

5.1. SUMMARY

This work was conducted in an attempt to investigate the hydrodynamics of HAHkT. The work was also performed in attempt to improve HAHkT performance when operating in river flow. Four sets of experiments on small HAHkT model were conducted in a water tunnel. The first three sets of experiments were used to investigate the power generated by turbine systems with different configurations. The power (torque multiplied by angular velocity) was collected by the mean of the torque and the RPM sensors. The collected data was then calculated in MATLAB scripts to generate the desired plot relationships. A 2D visual investigation of the flow within the downstream regions was conducted in the fourth set of experiments. Understanding the far wake region characteristics helps in optimizing the turbines arrangement in the multi-turbine system. A PIV system was used for this propose.

The HAHkTs used in this study contained either three or six untwisted, constant cross-section blades. The 3-blade turbines were tested in a water tunnel (for power generation) either singly or cooperatively in a multi-turbine system; either two or three rotors were mounted, coaxially, to the same shaft. These different 3- blade turbine arrangements were then shrouded with a duct reducer and tested again in the water tunnel. The 6-blade turbine was always tested singly and unshrouded for comparison. Various hydrodynamic parameters (e.g., pitch angle, number of blades, number of rotors, and TSR) were studied by monitoring the power curve response to these variables. The effects of flow velocity and applied load on turbine performance were also studied. The power curves generated by these different turbine system configurations were compared in attempt to better understand turbine optimization.

5.1.1. Power Evaluation.

5.1.1.1 The Effect of pitch angle and loaded torque. An unducted 3-blade single turbine was used to investigate the effect of pitch angle and loaded torque on extracted power. The generated power (P) was found to increase when the pitch angle decreased. The optimum pitch angle for the Eppler 395 hydrofoil was 5^{o}. The generated

power decreased (due to the stall effect) when the pitch angle was lower than 5^o . In general, decreasing the pitch angle from 20^o was always combined with increase in the rotor's angular velocity; however, the turbine tended to cut-out (when loaded) at lower flow velocities due to lower generated torque at these low pitch angles.

Considering TSR versus C_P , the power curve peak had a leftward shift and a lower magnitude when the pitch angle increased. In general, the C_P increased at all pitch angles as the TSR decreased because the AoA increased along the blade's length.

A 2D model of the hydrofoil was solved in CFD analysis. The results indicated that, the stall AoA is 12^o. This stall AoA could, however, be higher because the 2D problem did not take into account the effect of either centrifugal or Coriolis forces produced by the blade's rotation.

Increasing the applied torque had a positive effect on the turbine's performance by forcing the turbine to slow down, lowering its angular velocity, and thus increasing the AoA which in turn yielded higher lift.

5.1.1.2 The effect of flow operating conditions. The turbine was able to generate more power due to the higher energy flux that passed through its rotor when the flow velocity was increased. However, the power coefficient (C_P) decreased due to the decrease in AoA. This decrease in AoA was attributed to the higher rate of increase in the turbine angular velocity compared to the increased axial flow velocity.

5.1.1.3 The effect of increasing the number of blades and rotors. Both the two 3-blade turbine system and the 6-blade single turbine cut-in earlier and generated a higher power at the low flow regions than did the 3-blade single turbine. In contrast, the 3-blade single turbine was able to generate, comparatively, a higher power at high flow regions. The difference in the cut-in speed between either the 6-blade turbine or the multi-turbine system and the 3-blade single turbine increased as the applied torque increased. Improving the turbine performance at lower flow velocities increase the river's potential, particularly in slow flow streams.

Both the two 3-blade turbine system and the 6-blade single turbine reached a C_p that was higher than that of the 3-blade single turbine. This finding was expected as the

turbines with more blades had a larger blade area facing the flow, thus producing higher lift (torque). Lower operational TSR (TSR at maximum performance) was observed in these systems that had more blades or rotors. The decrease in operational TSR may be attributed to the slower flow that passed the system's rotor swept area due to the higher flow impedance, preventing the turbine form operating at stall AoA.

The power coefficient curve had the same behavior when the number of rotors was increased from two to three as it was when the number of rotors was increased from one to two. However, the performance improved less in the case the number of rotors was increased from two to three. This increase was smaller because the third rotor operated at a lower flow velocity than the second one (the velocity deficit behind the two rotors was higher than it was behind one rotor).

Both the 6-blade turbine and the two 3-blade turbine systems generated almost identical power curves with a slight down shift for the power curve generated by the latter. This small down shift occurred because the second rotor operated at a lower flow velocity. Moreover, the hub diameter of the 6-blade turbine was slightly larger than the 3-blade turbine which increased the diameter of the turbine. The gap between the two curves decreased as the flow velocity increased.

The power output generated by the multi-turbine system improved as the axial distance (x) between the system's rotors increased. The rotors' relative instillation angles (∅) had no effect on the turbine system when the axial distance between the rotors was 4D. However, when the axial distance set to 2D, the system with $\emptyset = 30^{o}$ generated higher power at lower flow velocities than it did with $\emptyset = 0^{o}$.

5.1.1.4 The effect of duct reducer. The output power produced by the ducted turbines increased due to the increased flow velocity passing through the rotors. The duct's nozzle accelerated the flow which in turn increase the kinetic energy flux that harvested by the turbine. For 3-blade single turbine, an improvement of maximum reached C_p , before turbine cut-out, was observed to be ranged between 260 to 310% for different inflow velocities ranged between 0.7272 to 0.9789 $\mathrm{m/s}$. The multi-turbine system did not achieve the maximum C_p because the clutch's capability was limited.

A general trend was observed for both single turbine and multi-turbine systems. The ducted turbine system's power curves shifted drastically more to the right (at higher TSR) than did the unducted turbine systems.

No power peak was reached because the turbine cut-out as the turbine angular velocity decreased. (The angular velocity decreased when the load on the turbine increased.) This phenomenon could be attributed to the stall delay, which is affected by centrifugal forces, hydrofoil shape, and angle of attacks at a local section along the blade's span [64].

5.1.2. Wake Investigation. In general, the wake's width increased and the axial velocity deficit decreased as the flow traveled further away from the turbine.

The velocity deficit behind the 6-blade turbine was higher than that behind the 3-blade turbine. This difference likely occurred because when the number of blades increased (and thus the solidity also increased), the flow impedance also increased. The velocity deficit resulted from the 6-blade turbine shows faster rate of recovery compared to the 3-blade turbine.

The normalized normal velocity component in the wake regions was smaller than the normalized axial velocity component. This indicated that the axial velocity was the dominate velocity component in determining the extracted power.

Increasing the free stream velocity shifted the velocity profile, inside the wake, to higher values. However, the axial velocity deficit (U/U_∞) for various free flow speeds had a similar profile trend. The flow deficit (the wake characteristics) was poorly affected by the incoming free stream velocity.

5.2. FUTURE WORK

5.2.1. Investigate the Effect of Varying Pitch Angle of Multi-turbine System. During this study, the pitch angle was kept the same for all the multi-turbine system's rotors. Thus, the AoA at the second rotor was smaller than that at the first one and so on so forth. The decrease in AoA was attributed to the decrease in axial flow (within the wake) caused by the rotors while maintaining the same angular velocity for all the

system's rotors. Therefore, decreasing the second and third rotor's pitch angle to values that optimize the AoA will increase the overall system efficiency.

5.2.2. Performing Computational Fluid Dynamics (CFD). The experimental investigation and optimization of hydrokinetic turbine is time consuming because a considerable number of experiments is required. A 3-D numerical CFD modeling method is more efficient in terms of cost, time, and details (e.g., pressure, thrust, lift, and drag forces around the blade). The experimental results can be used to validate the numerical simulation. The effect of hydrodynamic parameters (e.g., solidity, number of blades and rotors, and pitch angle) on the turbine system performance can then be deeply investigated.

APPENDIX A.
TIME-AVERAGE RPM SENSOR LABVIEW CODE

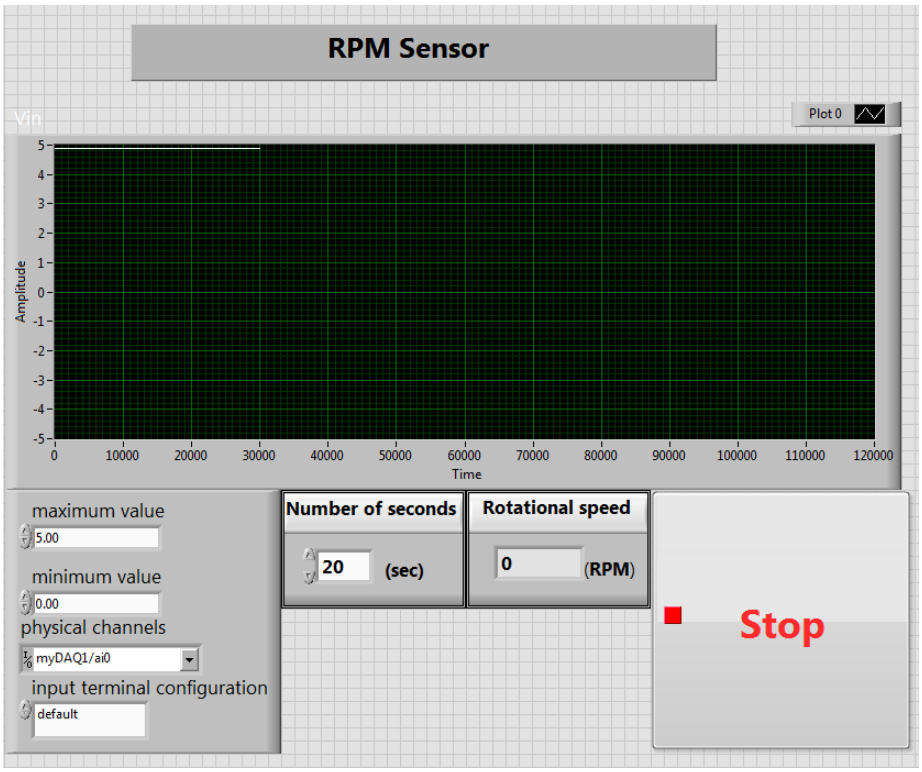

Figure A – 1. Time-Average RPM sensor LabVIEW front panel

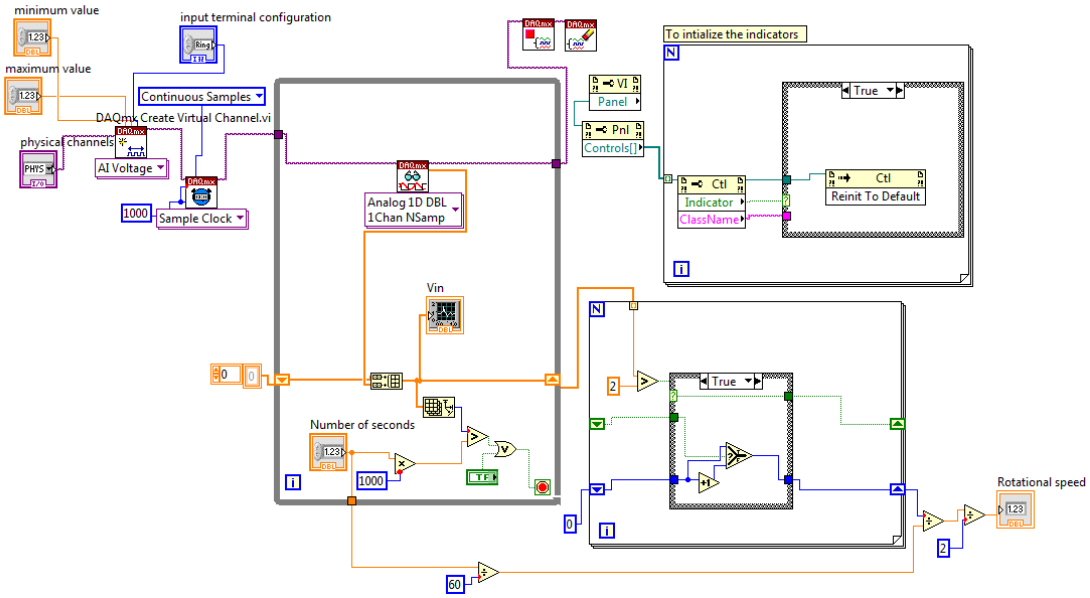

Figure A – 2. Time-Average RPM sensor LabVIEW block diagram

APPENDIX B.

EXPERIMENTAL RESULTS CALCULATION AND PLOTTING

```
% This code was generated for the following purposes
%1)Gives the user a list of cases to choose from.
%2)Calculate all the requirements
%3)Gives the user a list of relationships to plot.
clear all
close all
clc
% Constants needed for calculation
R=0.10954; % R is the radius of the rotor [m]
rho=997.0479; % 997.0479  is water density at 25C [kg/m^3]
 A=pi*R^2; % A is the The swept area by the rotor [m^2]
 tolerance=0.000001;% will be used for deleting zero elements to avoid miss
plotting results
%-------------------------------------------------------------------------
%Defining the generated power and corresponding RPM and flow speed matrices
%Pitch angle of 20 was maintained
%--------3-blade unducted turbine ----------------------------------------
Power{1}= xlsread('Power_RPM_Effect_New.xlsx','Pitch_20_1T','CF7:Cx10');
W_{1}=xlsread('Power_RPM_Effect_New.xlsx','Pitch_20_1T','E7:W10');
U{1}(:,1)= xlsread('Power_RPM_Effect_New.xlsx','Pitch_20_1T','CD7:CD10');

%------ 6-blade unducted turbine ----------------------------------------
Power{2}=
xlsread('Power_RPM_Effect_New.xlsx','Pitch_20_1T_6BLades','DO7:ET10');
W_{2}= xlsread('Power_RPM_Effect_New.xlsx','Pitch_20_1T_6BLades','E7:AJ10');
U{2}(:,1)=xlsread('Power_RPM_Effect_New.xlsx','Pitch_20_1T_6BLades','DM7:DM10')
;

%-------3-blade ducted turbine ------------------------------------------
Power{3}= xlsread('Power_RPM_Effect_New.xlsx','Pitch_20_Duct','DO7:EV10');
W_{3}= xlsread('Power_RPM_Effect_New.xlsx','Pitch_20_Duct','E7:AL10');
U{3}(:,1)= xlsread('Power_RPM_Effect_New.xlsx','Pitch_20_Duct','DM7:DM10');

%-------Two 3-blade ducted turbine --------------------------------------
Power{4}= xlsread('Power_RPM_Effect_New.xlsx','Pitch_20_2T_Duct','CQ8:DP11');
W_{4}= xlsread('Power_RPM_Effect_New.xlsx','Pitch_20_2T_Duct','E8:AD11');
U{4}(:,1)= xlsread('Power_RPM_Effect_New.xlsx','Pitch_20_2T_Duct','CO8:CO11');

%------ 3-blades multi-turbine system  ----------------------------------
% The x is the axial distance between rotors ans phi is rotors relative
% angle of installation
%Power_20_2Rotors_1: is 2-Turbines x=2D Phi= 0
%Power_20_2Rotors_2: is 2-Turbines x=2D Phi=30
%Power_20_2Rotors_3: is 2-Turbines x=4D Phi= 0
%Power_20_2Rotors_4: is 2-Turbines x=4D Phi=30
%Power_20_3Rotors_5: is 3-Turbines x=2  Phi=30

%Define the Power  matrix for all cases with  pitch angle 20
Power{5}=xlsread('Power_RPM_Effect_New.xlsx','Pitch_20_2T_2D_zeroAng','CX7:DY10
');
Power{6}=xlsread('Power_RPM_Effect_New.xlsx','Pitch_20_2T_2D_30Ang','CX7:DZ10')
;
Power{7}=xlsread('Power_RPM_Effect_New.xlsx','Pitch_20_2T_4D_zeroAng','DA7:ED10
');
Power{8,
#186}=xlsread('Power_RPM_Effect_New.xlsx','Pitch_20_2T_4D_30Ang','DH7:EM10');
Power{9}=xlsread('Power_RPM_Effect_New.xlsx','Pitch_20_3T_2D_30Ang','DQ7:EY10')
;

%Define the rotational speed matrix for all cases with  pitch angle 20
W_{5}=xlsread('Power_RPM_Effect_New.xlsx','Pitch_20_2T_2D_zeroAng','E7:AF10');
W_{6}= xlsread('Power_RPM_Effect_New.xlsx','Pitch_20_2T_2D_30Ang','E7:AG10');
W_{7}=xlsread('Power_RPM_Effect_New.xlsx','Pitch_20_2T_4D_zeroAng','E7:AH10');
```

```
W_{8,  #186}=
xlsread('Power_RPM_Effect_New.xlsx','Pitch_20_2T_4D_30Ang','E7:AJ10');
W_{9}= xlsread('Power_RPM_Effect_New.xlsx','Pitch_20_3T_2D_30Ang','E7:AM10');

%Define the flow speed matrix for all cases with  pitch angle 20
U{5}(:,1)=xlsread('Power_RPM_Effect_New.xlsx','Pitch_20_2T_2D_zeroAng','CV7:CV1
0');
U{6}(:,1)=xlsread('Power_RPM_Effect_New.xlsx','Pitch_20_2T_2D_30Ang','CV7:CV10'
);
U{7}(:,1)=xlsread('Power_RPM_Effect_New.xlsx','Pitch_20_2T_4D_zeroAng','CY7:CY1
0');
U{8,
#186}(:,1)=xlsread('Power_RPM_Effect_New.xlsx','Pitch_20_2T_4D_30Ang','DF7:DF10
');
U{9}(:,1)=xlsread('Power_RPM_Effect_New.xlsx','Pitch_20_3T_2D_30Ang','DO7:DO10'
);

%--------------Investegation of Pitch angle effect-------------------------
%Define rpower matrix for single turbien with diferent pitch angles
Power{10} = xlsread('Power_RPM_Effect_New.xlsx','Pitch_5','CC7:CU10');
Power{11,  #39} = xlsread('Power_RPM_Effect_New.xlsx','Pitch_17','CC7:CQ10');
Power{12,  #51} = xlsread('Power_RPM_Effect_New.xlsx','Pitch_20','CC7:CO10');

%Define rotational speed matrix for single turbien with diferent pitch angles
W_{10} = xlsread('Power_RPM_Effect_New.xlsx','Pitch_5','E7:W10');
W_{11,  #39}= xlsread('Power_RPM_Effect_New.xlsx','Pitch_17','E7:S10');
W_{12,  #51} = xlsread('Power_RPM_Effect_New.xlsx','Pitch_20','E7:Q10');
%Define flow speed matrix for single turbin with different pitch angles
U{10}(:,1) = xlsread('Power_RPM_Effect_New.xlsx','Pitch_5','CA7:CA10');
U{11,  #39}(:,1) = xlsread('Power_RPM_Effect_New.xlsx','Pitch_17','CA7:CA10');
U{12,  #51}(:,1) = xlsread('Power_RPM_Effect_New.xlsx','Pitch_20','CA7:CA10');
for G=1:5
  fprintf(2,'List to choose from. Note that Multi-Turbine cases numbered from 5
to 9 \n')
 fprintf('\n   Please note all system cases are tested at  Pitch Angle of 20
except the last three ');
 fprintf('\n 1. 3-Blades Unducted Turbine')
 fprintf('\n 2. 6-Blades Unducted Turbine\n')
 fprintf('\n 3. 3-Blades Ducted Turbine ')
 fprintf('\n 4. Two 3-Blades Ducted Turbines, 2 Diameter Apart, rotors
installation Angle is 30\n')
 fprintf('\n 5. Two 3-Blades Unducted Turbines, 2 Diameter Apart, rotors
installation Angle is zero ')
 fprintf('\n 6. Two 3-Blades Unducted Turbines, 2 Diameter Apart, rotors
installation Angle is 30')
 fprintf('\n 7. Two 3-Blades Unducted Turbines, 4 Diameter Apart, rotors
installation Angle is zero')
 fprintf('\n 8. Two 3-Blades Unducted Turbines, 4 Diameter Apart, rotors
installation Angle is 30')
 fprintf('\n 9. Three 3-Blades Unducted Turbines, 2 Diameter Apart, rotors
installation Angle is 30\n\n')
 fprintf(2,'List to choose from. Pitch angle investigation \n')
 fprintf('\n 10. 3-Blades Unducted Turbine with Pitch Angle of 5')
 fprintf('\n 11. 3-Blades Unducted Turbine with Pitch Angle of 17')
 fprintf('\n 12. 3-Blades Unducted Turbine with Pitch Angle of 20\n\n')
  J = input('Enter cases numbers you consider between [ ] \n');
% Calculation of tip speed ratio (TSR)
 for i=1:length(J) % i is index for the chossen cases
  TS{i}=vpa((W_{J(i)}*2*pi*R/60));
  m=size(TS{i},2);
  n=size(TS{i},1);
    for j=1:m
    for k=1:n
```

```
     TSR{i}(k,j)=double(TS{i}(k,j)/U{J(i)}(k,1));
    end
    end
 % Calculation of power coefficient Cp
% x_TSR{i}=zeros(n,m);
y_Cp{i}=zeros(n,m);y_P{i}=zeros(n,m);x_RPM{i}=zeros(n,m);
  cp{i}=vpa((Power{J(i)}/(0.5*rho*A)));
  m=size(cp{i},2);
  n=size(cp{i},1);
    for j=1:m
      for k=1:n
     Cp{i}(k,j)=double(cp{i}(k,j)/((U{J(i)}(k,1))^3));
     end
    end
% To plot Power and Cp vs.TSR
x_TSR{i}=TSR{i}    ;y_Cp{i}=Cp{i};
x_TSR_2{i}=TSR{i}  ;y_P{i}=Power{J(i)};

% % To plot the P vs. RPM
x_RPM{i}=W_{J(i)} ; y_P_2{i}=Power{J(i)};
 end
%%%%%%%%%%%%%%%%%%%%%%%%%%%%%%%%%%%%%%%%%%%%%%%%%%%%%%%%%%%%%%%%%%%%%%%%%%%%

 plotStyle1 = {'^k','ok','sk','<k','hk','vk','dK'};
 plotStyle2 = {'^k','ok','sk','<k','hk','vk','dK'};
 plotStyle3 = {':','^k',':','ok',':','sk',':','dk',':','hk',':','vk',':','<K'};
 plotStyle4 = {'^k',':','ok',':','sk',':','dk',':','hk',':','vk',':','<K'};

Case_Name={'Unducted 3-Blade Single Turbine','Unducted 6-Blade Single
Turbine','Ducted 3-Blade Single Turbine',...
'Ducted Two 3-Blade Turbines (x =2D, \phi=30^{\circ}) ','Unducted Two 3-Blade
Turbines (x =2D, \phi=0^{\circ})',...
'Unducted Two 3-Blade Turbines (x =2D, \phi=30^{\circ})','Unducted Two 3-Blade
Turbines (x =4D, \phi=0^{\circ})',...
'Unducted Two 3-Blade Turbines (x =4D, \phi=30^{\circ})','Unducted Three 3-
Blade Turbines (x =2D, \phi=30^{\circ})',...
'Pitch Angle=5^{\circ}','Pitch Angle=17^{\circ}','Pitch Angle=20^{\circ}'};

fprintf('\n 1. Plot generated power and power coeficient vs TSR for every case
separately at particular flow speed ');
fprintf('\n 2. Plot and compare the power vs TSR for the selected cases at
fixed speed ');
fprintf('\n 3. Plot and compare the power coefficient vs TSR for the selected
cases at fixed speed ');
fprintf('\n 4. Plot generated power vs RPM for each case at different flow
speeds\n');
fprintf(2,' 5. No plotting is required ');
PLOT=input('\n Inter the number of relationship you want to plot\n');
switch PLOT
  case{1}
%Plot power generated and power coeficient vs TSR for every case separately at
particular flow speed
  close all;tt=1;
for i=1:length(J)
for j=1:n
     figure(tt)
[AX,H1,H2] = plotyy(x_TSR_2{i}(j,:),y_P{i}(j,:),x_TSR{i}(j,:),y_Cp{i}(j,:),...
@(X,Y) plot(X,Y,plotStyle1{1}), @(X,Y) plot(X,Y,plotStyle2{1}));
set(get(AX(1),'Ylabel'),'String',' Power (W)');
set(get(AX(2),'Ylabel'),'String','Power Coefficient (Cp)');
xlabel('TSR');
set(H1,'MarkerFaceColor','k');
```

```
title({[' Generated Power and Power Coefficient vs. TSR for
',Case_Name{J(i)}];...
[' with Pitch Angle of 20^{\circ} and Flow Speed of ',num2str(U{J(i)}(j,1)),'
(m/s)']});
legend('Power','Cp');  set(gcf, 'Color', ones(1, 3));grid on;
tt=tt+1;
end
end
case{2}
% Plot and compare the power vs TSR for selected cases at fixed speed
 close all;tt=1;
for j=1:n
    figure(tt);
    for i=1:length(J)
    if mod(i,2) == 0
plot(x_TSR_2{i}(j,:),y_P{i}(j,:),plotStyle3{i},'MarkerFaceColor','k');
    else
    plot(x_TSR_2{i}(j,:),y_P{i}(j,:),plotStyle4{i});
    end
xlabel('TSR');ylabel('Power (W)');
if (J(1)==10 || J(1)==11 || J(1)==12 || J(2)==10 || J(2)==11 || J(2)==12 ||
J(2)==10 || J(2)==11 || J(2)==12);
title(['Power vs. TSR for  Flow Speed of ',num2str(U{J(i)}(j,1)), ' (m/s)']);
legendInfo{i}=[Case_Name{J(i)}];set(gcf, 'Color', ones(1, 3));grid on;
 hold on
else
title(['Power vs. TSR for Pitch Angle of 20^{\circ} and Flow Speed of
',num2str(U{J(i)}(j,1)), ' (m/s)']);
legendInfo{i}=[Case_Name{J(i)}];set(gcf, 'Color', ones(1, 3));grid on;
 hold on
end
    end
    legend(legendInfo)
 hold off
 set(legend,'Location','NorthWest')
 tt=tt+1;
end
case{3}
% Plot and compare the power coefficient vs TSR for selected cases at fixed
speed
 close all;tt=1;
for j=1:n
    figure(tt)
    for i=1:length(J)
    if mod(i,2) == 0
  plot(x_TSR{i}(j,:),y_Cp{i}(j,:),plotStyle3{i},'MarkerFaceColor','k');
    else
  plot(x_TSR{i}(j,:),y_Cp{i}(j,:),plotStyle4{i});
    end
xlabel('TSR');ylabel('Power coefficient (C_p)');
if (J(1)==10 || J(1)==11 || J(1)==12 || J(2)==10 || J(2)==11 || J(2)==12 ||
J(2)==10 || J(2)==11 || J(2)==12);
title(['Power Coefficien vs. TSR for  Flow Speed of ',num2str(U{J(i)}(j,1)), '
(m/s)']);
legendInfo{i}=[Case_Name{J(i)}];set(gcf, 'Color', ones(1, 3));grid on;
 hold on
else
title(['Power Coefficient vs. TSR for Pitch Angle of 20^{\circ} and Flow Speed
of ',num2str(U{J(i)}(j,1)),' (m/s)']);
legendInfo{i}=[Case_Name{J(i)}];set(gcf, 'Color', ones(1, 3));grid on;
 hold on
end
 set(legend,'Location','SouthWest')
```

```
    end
    legend(legendInfo)
 hold off
 tt=tt+1;
end
case{4}
% Plot generated power vs RPM for each case at different flow speeds
     close all;tt=1;
fprintf('\n 1.Plot without operation optimized curve ');
 fprintf('\n 2.Plot with using operation optimized curve ');
Opt=input('\n enter the number of prefered case listed above and press
enter\n');
switch Opt
  case{1} % no optimization
 for i=1:length(J)
     figure(tt)
 for j=1:n
    if mod(j,2) == 0
plot(x_RPM{i}(j,:),y_P_2{i}(j,:),plotStyle3{j},'MarkerFaceColor','k');
    else
    plot(x_RPM{i}(j,:),y_P_2{i}(j,:),plotStyle4{j});
    end
xlabel('Rotational Speed (RPM)');ylabel('Power (W)');
title({[' Generated Power  vs. RPM '];['for ',Case_Name{J(i)},' with Pitch
Angle of 20^{\circ}']});
legendInfo{j}=['U=' num2str(U{J(i)}(j,1)),' (m/s)'];grid on;set(gcf, 'Color',
ones(1, 3));grid on;
 hold on
 end
 legend(legendInfo)
 hold off
 tt=tt+1;
 end
  case{2} % with optimized curve
    for i=1:length(J)
     figure(tt)
 for j=1:n
    if mod(j,2) == 0
plot(x_RPM{i}(j,:),y_P_2{i}(j,:),plotStyle3{j},'MarkerFaceColor','k');
    else
    plot(x_RPM{i}(j,:),y_P_2{i}(j,:),plotStyle4{j});
    end
xlabel('Rotational Speed (RPM)');ylabel('Power (W)');
%title({[' Generated Power  vs. RPM '];['for ',Case_Name{J(i)},' with Pitch
Angle of 20^{\circ}']});
legendInfo{j}=['U=' num2str(U{J(i)}(j,1)),' (m/s)'];grid on;set(gcf, 'Color',
ones(1, 3));grid on;
 hold on
end
  plot(RPM_max{i},P_max{i},'ok');
  legend(legendInfo)
  hold off
 tt=tt+1;
    end
 end
case{5}
 error('No Plot Needed')
end
end
```

BIBLIOGRAPHY

[1] S. Bilgen, S. Keleş, A. Kaygusuz, A. Sarı, and K. Kaygusuz, "Global warming and renewable energy sources for sustainable development: A case study in Turkey," *Renewable and Sustainable Energy Reviews,* vol. 12, pp. 372-396, 2008.

[2] http://www.eia.gov/forecasts/ieo/electricity.cfm. *INTERNATIONAL ENERGY OUTLOOK 2013. (last accessed April 2014).*

[3] P. Frankl, "RENEWABLE ENERGY COMING OF AGE," *INTERNATIONAL ENERGY AGENCY,* p. 3, 2012.

[4] "WORLD ENERGY OUTLOOK 2010," *INTERNATIONAL ENERGY AGENCY*, 2010.

[5] M. Kaltschmitt, W. Streicher, and A. Wiese, *Renewable energy: technology, economics and environment*: Springer, 2007.

[6] http://www.eia.gov/forecasts/aeo/er/pdf/0383er%282014%29.pdf. *AEO2014 EARLY RELEASE OVERVIEW. (last accessed April 2014).*

[7] N. Lior, "Energy resources and use: the present situation and possible paths to the future," *Energy,* vol. 33, pp. 842-857, 2008.

[8] M. Güney and K. Kaygusuz, "Hydrokinetic energy conversion systems: A technology status review," *Renewable and Sustainable Energy Reviews,* vol. 14, pp. 2996-3004, 2010.

[9] "WorldEnergyOutlook2010," *INTERNATIONAL ENERGY AGENCY*, 2010.

[10] http://oceanenergy.epri.com/. *Overview of U.S. Ocean Wave and Current Energy. (last accessed April 2014).*

[11] http://www.nrel.gov/docs/fy13osti/54909.pdf. *2011 Renewable Energy Data Book. (last accessed April 2014).*

[12] D. Hall, K. Reeves, J. Brizzee, R. Lee, G. Carroll, and G. Sommers, "Wind and hydropower technologies, feasibility assessment of the water energy resources of the United States for new low power and small hydro classes of hydroelectric plants," *Idaho National Laboratory*, 2006.

[13] C. Lawn, "Optimization of the power output from ducted turbines," *Proceedings of the Institution of Mechanical Engineers, Part A: Journal of Power and Energy,* vol. 217, pp. 107-117, 2003.

[14] http://www.windustry.org/resources/how-much-do-wind-turbines-cost. *How much do wind turbines cost? (last accessed April 2014).*

[15] A. Bahaj and L. Myers, "Fundamentals applicable to the utilisation of marine current turbines for energy production," *Renewable Energy*, vol. 28, pp. 2205-2211, 2003.

[16] "Hydrokinetic Turbines in Canals: Potential and Reality," *Seattle,WA*.

[17] M. J. Khan, G. Bhuyan, M. T. Iqbal, and J. E. Quaicoe, "Hydrokinetic energy conversion systems and assessment of horizontal and vertical axis turbines for river and tidal applications: A technology status review," *Applied Energy*, vol. 86, pp. 1823-1835, 2009.

[18] http://www.enchantedlearning.com/usa/rivers/. *US Rivers. (last accessed April 2014).*

[19] http://www.energy.gov/. *Assessment and Mapping of the Riverine Hydrokinetic Resource in the Continental United States. (last accessed April 2014).*

[20] J. B. Johnson and D. J. Pride, "River, tidal and ocean current hydrokinetic energy technologies: Status and future opportunities in Alaska," *Prepared for Alaska Center for Energy and Power*, 2010.

[21] S. Subhra Mukherji, N. Kolekar, A. Banerjee, and R. Mishra, "Numerical investigation and evaluation of optimum hydrodynamic performance of a horizontal axis hydrokinetic turbine," *Journal of Renewable and Sustainable Energy*, vol. 3, p. 063105, 2011.

[22] M. J. Khan, M. T. Iqbal, and J. E. Quaicoe, "River current energy conversion systems: Progress, prospects and challenges," *Renewable and Sustainable Energy Reviews*, vol. 12, pp. 2177-2193, 2008.

[23] T. S. Reynolds, *Stronger than a hundred men: a history of the vertical water wheel*: JHU Press, 2002.

[24] A. Wilson, "Machines, power and the ancient economy," *Journal of Roman Studies*, vol. 92, pp. 1-32, 2002.

[25] L. Nash, "The Changing Experience of Nature: Historical Encounters with a Northwest River," *The Journal of American History*, vol. 86, pp. 1600-1629, 2000.

[26] I. S. Hwang, Y. H. Lee, and S. J. Kim, "Optimization of cycloidal water turbine and the performance improvement by individual blade control," *Applied Energy*, vol. 86, pp. 1532-1540, 2009.

[27] M. Khan, G. Bhuyan, M. Iqbal, and J. Quaicoe, "Hydrokinetic energy conversion systems and assessment of horizontal and vertical axis turbines for river and tidal applications: A technology status review," *Applied Energy*, vol. 86, pp. 1823-1835, 2009.

[28] R. H. Clark, *Elements of tidal-electric engineering* vol. 33: John Wiley & Sons, 2007.

[29] J. Zanette, D. Imbault, and A. Tourabi, "Fluid-structure interaction and design of water current turbines," in *the 2nd IAHR International Meeting of the Workgroup on Cavitation and Dynamic Problems in Hydraulc Machinery and Systems, Timisoara, Romania, October*, 2007, pp. 24-26.

[30] B. Kirke, "Developments in ducted water current turbines," *Tidal paper,* 2006.

[31] N. Kolekar, S. S. Mukherji, and A. Banerjee, "Numerical Modeling and Optimization of Hydrokinetic Turbine," in *Proceedings of ASME 2011 5th International Conference on Energy Sustainability and 9th Fuel Cell Science, Engineering & Technology Conference. Washington, DC, Paper*, 2011.

[32] M. Khan, M. T. Iqbal, and J. E. Quaicoe, "A technology review and simulation based performance analysis of river current turbine systems," in *Electrical and Computer Engineering, 2006. CCECE'06. Canadian Conference on*, 2006, pp. 2288-2293.

[33] L. I. Lago, F. L. Ponta, and L. Chen, "Advances and trends in hydrokinetic turbine systems," *Energy for Sustainable Development,* vol. 14, pp. 287-296, 2010.

[34] C. Lang, "Harnessing tidal energy takes new turn," *Spectrum, IEEE,* vol. 40, p. 13, 2003.

[35] H. Li, G. A. Taylor, A. M. Abutunis, K. Chandrashekhara, A. R. Kashyap, and J. W. Kimball, "DESIGN AND PERFORMANCE EVALUATION OF A HYDROKINETIC COMPOSITE TURBINE SYSTEM," presented at the SAMPE, Long Beach, CA, 2013.

[36] S. L. Dixon, *Fluid mechanics and thermodynamics of turbomachinery*: Butterworth-Heinemann, 2005.

[37] C. Thumthae and T. Chitsomboon, "Optimal angle of attack for untwisted blade wind turbine," *Renewable Energy,* vol. 34, pp. 1279-1284, 2009.

[38] M. O. Hansen, *Aerodynamics of wind turbines*: Routledge, 2013.

[39] M. S. Guney, "Evaluation and measures to increase performance coefficient of hydrokinetic turbines," *Renewable and Sustainable Energy Reviews,* vol. 15, pp. 3669-3675, 2011.

[40] D. C. Wilcox, *Basic fluid mechanics*: DCW industries, 2010.

[41] T. Burton, N. Jenkins, D. Sharpe, and E. Bossanyi, *Wind energy handbook*: John Wiley & Sons, 2011.

[42] M. M. Duquette and K. D. Visser, "Numerical Implications of Solidity and Blade Number on Rotor Performance of Horizontal-Axis Wind Turbines," *Journal of Solar Energy Engineering,* vol. 125, p. 425, 2003.

[43] A. Bahaj, L. Myers, M. Thomson, and N. Jorge, "Characterising the wake of horizontal axis marine current turbines," *Proc. 7th EWTEC,* 2007.

[44] L. J. Vermeer, J. N. Sørensen, and A. Crespo, "Wind turbine wake aerodynamics," *Progress in Aerospace Sciences,* vol. 39, pp. 467-510, 2003.

[45] L. P. Chamorro, D. R. Troolin, S.-J. Lee, R. E. A. Arndt, and F. Sotiropoulos, "Three-dimensional flow visualization in the wake of a miniature axial-flow hydrokinetic turbine," *Experiments in Fluids,* vol. 54, 2013.

[46] D.-m. Hu and Z.-h. Du, "Near Wake of a Model Horizontal-Axis Wind Turbine," *Journal of Hydrodynamics, Ser. B,* vol. 21, pp. 285-291, 2009.

[47] A. S. Bahaj, W. M. J. Batten, and G. McCann, "Experimental verifications of numerical predictions for the hydrodynamic performance of horizontal axis marine current turbines," *Renewable Energy,* vol. 32, pp. 2479-2490, 2007.

[48] R. Lanzafame and M. Messina, "Power curve control in micro wind turbine design," *Energy,* vol. 35, pp. 556-561, 2010.

[49] W. C. Schleicher, J. D. Riglin, Z. A. Kraybill, A. Oztekin, and R. C. Klein Jr, "DESIGN AND SIMULATION OF A MICRO HYDROKINETIC TURBINE."

[50] W. M. J. Batten, A. S. Bahaj, A. F. Molland, and J. R. Chaplin, "Hydrodynamics of marine current turbines," *Renewable Energy,* vol. 31, pp. 249-256, 2006.

[51] W. M. J. Batten, A. S. Bahaj, A. F. Molland, and J. R. Chaplin, "Experimentally validated numerical method for the hydrodynamic design of horizontal axis tidal turbines," *Ocean Engineering,* vol. 34, pp. 1013-1020, 2007.

[52] A. S. Bahaj, A. F. Molland, J. R. Chaplin, and W. M. J. Batten, "Power and thrust measurements of marine current turbines under various hydrodynamic flow conditions in a cavitation tunnel and a towing tank," *Renewable Energy,* vol. 32, pp. 407-426, 2007.

[53] C. Consul, R. Willden, E. Ferrer, and M. McCulloch, "Influence of solidity on the performance of a cross-flow turbine," in *8th European Wave and Tidal Energy Conference. Uppsala, Sweden*, 2009.

[54] M. C. Rector, K. D. Visser, and C. Humiston, "Solidity, Blade Number, and Pitch Angle Effects on a One Kilowatt HAWT," in *44th AIAA Aerospace Sciences Meeting and Exhibit*, 2006.

[55] F. Ponta and G. Shankar Dutt, "An improved vertical-axis water-current turbine incorporating a channelling device," *Renewable Energy*, vol. 20, pp. 223-241, 2000.

[56] F. Ponta and P. Jacovkis, "Marine-current power generation by diffuser-augmented floating hydro-turbines," *Renewable Energy*, vol. 33, pp. 665-673, 2008.

[57] B. Gilbert and K. Foreman, "Experiments with a diffuser-augmented model wind turbine," *Journal of Energy Resources Technology*, vol. 105, pp. 46-53, 1983.

[58] T. Setoguchi, N. Shiomi, and K. Kaneko, "Development of two-way diffuser for fluid energy conversion system," *Renewable Energy*, vol. 29, pp. 1757-1771, 2004.

[59] A. Nasution and D. W. Purwanto, "Optimized curvature interior profile for Diffuser Augmented Wind Turbine (DAWT) to increase its energy-conversion performance," in *Clean Energy and Technology (CET), 2011 IEEE First Conference on*, 2011, pp. 315-320.

[60] H. Xiao, L. Duan, R. Sui, and T. R¨osgen, "Experimental Investigations of Turbulent WakeBehind Porous Disks," *Marine Energy Technology Symposium*, 2013.

[61] http://download.ni.com/pub/devzone/tut/utsi-halleffect.pdf, "Hall Effect Sensor. (last accessed May 2014)."

[62] G. I. Comyn, D. S. Nobes, and B. A. Fleck, "Performance Evaluation and Wake Study of a Micro Wind Turbine," *Transactions of the Canadian Society for Mechanical Engineering*, vol. 35, pp. 101-117, 2011.

[63] C. Garrett and P. Cummins, "The efficiency of a turbine in a tidal channel," *Journal of Fluid Mechanics*, vol. 588, 2007.

[64] L. Myers and A. S. Bahaj, "Power output performance characteristics of a horizontal axis marine current turbine," *Renewable Energy*, vol. 31, pp. 197-208, 2006.

VITA

Abdulaziz M. Abutunis was born in Sebha, Libya. In May 1997, he received his B.S. with Honors in Mechanical Engineering from the Higher Institute of Engineering, Hoon, Libya. He did his summer training at Tripoli West power Planet in 1996. In March 1999, he joined as a Technical Engineer in a textile factory. During December 2007 - March 2008, he worked as an Assistant Engineer with CASON Engineering Plc. for water supply trail program in Libya.

In April 2008, Abdulaziz joined Higher Institute of Engineering, Hoon, Libya. He worked as a Laboratory Instructor until April 2010. He joined Missouri University of Science and Technology (Missouri S&T) in August 2011 in the Department of Mechanical and Aerospace Engineering. He worked as a Graduate Teaching Assistant at Missouri S&T. He graduated with a Master's Degree in Mechanical Engineering in December 2014.